NeuroImage 318 (2025) 121390

Contents lists available at ScienceDirect

NeuroImage

journal homepage: www.elsevier.com/locate/ynimg

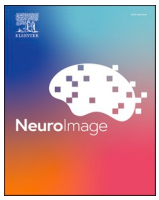

On the use of multi-echo NODDI MRI with released intrinsic diffusivity for the assessment of tissue diffusion and relaxation properties in experimental ischaemic stroke

Ezequiel Farrher [a,*], Kuan-Hung Cho [b,*], Chia-Wen Chiang [c], Ming-Jye Chen [c], Sheng-Min Huang [d], Li-Wei Kuo [c,e], Chang-Hoon Choi [a], N. Jon Shah [a,f,g,h]

[a] Institute of Neuroscience and Medicine 4, INM–4, Forschungszentrum Jülich, Germany
[b] Department of Electronic Engineering, National United University, Miaoli, Taiwan
[c] Institute of Biomedical Engineering and Nanomedicine, National Health Research Institutes, Miaoli, Taiwan
[d] Department of Pharmacology, College of Medicine, National Cheng Kung University, Tainan, Taiwan
[e] Institute of Medical Device and Imaging, National Taiwan University College of Medicine, Taipei, Taiwan
[f] Department of Neurology, RWTH Aachen University, Aachen, Germany
[g] JARA – BRAIN – Translational Medicine, Aachen, Germany
[h] Institute of Neuroscience and Medicine 11, INM–11, JARA, Forschungszentrum Jülich, Germany

ARTICLE INFO

Keywords:
Stroke
Ischaemia
MCAo
NODDI
MTE-NODDI
Diffusion MRI
Intrinsic diffusivity
Tissue microstructure
Transverse relaxation
Multi-compartment model
Multi-dimensional MRI

ABSTRACT

The multi-echo neurite orientation dispersion and density imaging (MTE-NODDI) model has been proposed to overcome one of the shortcomings of conventional NODDI, namely the echo time (TE) dependence of the compartmental signal fractions, which stems from the intrinsic differences in the compartmental transverse relaxation times (T2). However, the model continues to be constrained by the limitation of having a fixed, brain-wide intrinsic diffusivity, *d*.

The primary aim of this work is to assess the benefits and shortcomings of using MTE-NODDI to investigate the diffusion and T2 properties of ischaemic stroke tissue following middle cerebral artery occlusion (MCAo) in rat models. Given the known alterations in the diffusion properties in ischaemic tissue, a secondary aim is to assess an estimation approach for MTE-NODDI parameters that enables *d* to be released while also mitigating the consequent model degeneracy. Using the MTE-NODDI parameters, the spatiotemporal evolution of diffusion and T2 properties in ischaemic tissue was characterised from day one to day 23 post-MCAo. The proposed approach enables access to several unique tissue features that would otherwise be obscured by the conventional approach. Importantly, a marked reduction in *d* was observed, leading to significant changes in other MTE-NODDI parameters compared to the model employing a fixed *d*. The isotropic signal fraction displayed a significant increase in ischemic tissue, which appears in contradiction with previous works. Regarding the intra- and extra-neurite T2 values, $T_{2,\mathrm{in}}$ and $T_{2,\mathrm{en}}$, a significant increment was observed at the ischaemic tissue, while the condition $T_{2,\mathrm{in}} \geq T_{2,\mathrm{en}}$ displayed a tendency to hold in both tissue types. More generally, some parameters, such as the isotropic signal fraction, the intrinsic diffusivity and both compartmental T2 values, display unique, heterogeneous spatiotemporal evolution, where the core and border zones of the ischaemic tissue show different behaviours. Overall, the newly estimated parameters show greater consistency with analogous estimates reported by published models, and are anticipated to significantly enhance the understanding of tissue properties following ischaemic stroke.

Abbreviation: NODDI, neurite orientation dispersion and density imaging; TE, echo time; MTE, multi-echo time; MCAo, middle cerebral artery occlusion; DW, diffusion-weighted; T2W, transverse-relaxation-weighted; WM, white matter; GM, grey matter; ODI, orientation dispersion index; TR, repetition time; FOV, field of view; MSE, mean squared error; DTIT2, diffusion tensor imaging with explicit account for T2 relaxation; ROI, region of interest; FA, fractional anisotropy; SEM, standard error of the mean; AD, axial diffusivity; RD, radial diffusivity; SNR, signal-to-noise ratio; MD, mean diffusivity; CSF, cerebrospinal fluid; DKI, diffusion kurtosis imaging.

* Corresponding authors.
E-mail addresses: e.farrher@fz-juelich.de (E. Farrher), khcho@nuu.edu.tw (K.-H. Cho).

https://doi.org/10.1016/j.neuroimage.2025.121390
Received 13 January 2025; Received in revised form 9 July 2025; Accepted 22 July 2025
Available online 24 July 2025

1. Introduction

Diffusion-weighted (DW) and transverse-relaxation-weighted (T2W) MRI are two of the most widely used modalities for characterising brain tissue from the hyperacute to the chronic phases of ischaemic stroke. DW MRI, in particular, has become the preferred method for spatial localisation and assessment of the ischaemic zone during the hyperacute and acute phases due to its exquisite sensitivity to microstructural changes following stroke onset, such as the formation of cytotoxic oedema, changes in membrane permeability, neurite beading and tissue vacuolation (Budde and Frank, 2010; DiBella et al., 2022; Farrher et al., 2021; Grinberg et al., 2014, 2012; Hui et al., 2012b, 2012a; Jensen et al., 2011; Knight et al., 1991; Lätt et al., 2009; Moseley et al., 1990; Sotak, 2002). Moreover, the conventional transverse relaxation time (T2) has been shown to be sensitive to mechanisms such as vasogenic oedema, the increase in the binding of free water by degraded supramolecular structures and tissue liquefaction (Carano et al., 2000; Knight et al., 2016; Lin et al., 2002; Lin et al., 2002; Ordidge et al., 1991; Wagner et al., 2012). However, the relation between these mechanisms and their manifestation in the spatiotemporal dynamics of DW and T2W MRI biomarkers remains a topic of debate.

Among the various biophysical models for DW MRI signal, neurite orientation dispersion and density imaging (NODDI) has been widely used in the literature due to its enhanced sensitivity to tissue microstructural features, such as neurite density (or signal fraction) and orientation dispersion, and its clinically practicable scan times (Kamiya et al., 2020; Zhang et al., 2012). NODDI has been applied in a wide range of studies, including those on Alzheimer's (Colgan et al., 2016) and Parkinson's (Kamagata et al., 2016) diseases, multiple sclerosis (Crombe et al., 2018) and traumatic brain injury (Gazdzinski et al., 2020).

In the NODDI model, the total DW MRI signal is expressed as the sum of three non-exchanging compartments, namely, the isotropic (or free) water, and the intra- and extra-neurite (axons and dendrites) compartments. It further assumes that the axial, intra- and extra-neurite diffusivities are equal, normally referred to as intrinsic diffusivity (Guerrero et al., 2019). Moreover, the radial diffusivity in the extra-neurite compartment is assumed to be linked to the axial diffusivity and the intra-neurite signal fraction via a tortuosity model (Szafer et al., 1995; Zhang et al., 2012). Critically, in order to address the degeneracy in NODDI parameter estimation, the intrinsic diffusivity, d, is conventionally fixed to a brain-wide value typically set at 1.7 μm^2/ms (Zhang et al., 2012). However, this value is known to be an approximation and is only optimised for white matter (WM), whereas other values have been suggested for grey matter (GM), $d = 1.1$ μm^2/ms (Fukutomi et al., 2018), or *post mortem* rat brain tissue, $d = 1.2$ μm^2/ms (Crombe et al., 2018). More generally, previous studies have questioned the validity of assuming a fixed d value across the brain. For example, Guerrero et al. (2019) proposed a voxel-wise estimation framework where the optimal d was determined by first evaluating the model square residuals for a range of plausible d values and subsequently performing a linear search along the d-dimension. Their results showed that d is indeed spatially dependent and, as a consequence, restricting it to a fixed value for the whole brain can lead to a bias in the other NODDI parameters. Similarly, Howard et al. (2022) estimated the axial intra-neurite diffusivity in WM by using high diffusion weightings (b-values) to suppress the signal of the extra-neurite compartment, and revealed that even within WM, the intra-neurite diffusivity is spatially dependent, with values reaching ~2.4 μm^2/ms. Crucially, the compartmental diffusivities have been shown to significantly change in ischaemic tissue using similar models (Hui et al., 2012b; Kellner et al., 2022), whereas a reduction in the intra-neurite diffusivity has been predicted by a theoretical model (Budde and Frank, 2010) built on experimental evidence. Furthermore, in a recent work (Farrher et al., 2023), the authors demonstrated that fixing d to a value significantly greater than the underlying substrate may subsequently lead to biologically implausible values for the intra-neurite signal fraction. Hence, the several works devoted to investigate ischemic stroke with conventional NODDI in the literature, both in human and preclinical studies (Adluru et al., 2014; Bagdasarian et al., 2021; Caverzasi et al., 2016; Hodgson et al., 2019; Kamiya et al., 2020; Mastropietro et al., 2019; Wang et al., 2019; Wang et al., 2021), may entail, in spite of the reported sensitivity, jeopardised specificity.

Another limitation of multi-compartment DW MRI models, such as NODDI, is the echo time (TE) dependence of the compartmental signal fractions. This stems from the intrinsic differences in compartmental T2 values, coupled with the use of single-TE experiments (Benjamini and Basser, 2017; Collier et al., 2018; Farrher et al., 2020; Gong et al., 2020; Lampinen et al., 2019; Veraart et al., 2017). For example, cerebrospinal fluid (CSF) is known to have T2 values significantly larger than those of tissue, which leads to an overestimation of the free-diffusion water fraction in various models (Bouyagoub et al., 2016; Collier et al., 2018; Farrher et al., 2021, 2020; Pasternak et al., 2009). Similarly, the intra-neurite T2 is generally larger, though to a lesser extent, than that of the extra-neurite compartment in WM (Benjamini and Basser, 2017; Gong et al., 2020; McKinnon and Jensen, 2019; Peled et al., 1999; Veraart et al., 2017). Conversely, the distinction in GM remains an area of debate (Benjamini and Basser, 2017; Dortch et al., 2010; Gong et al., 2020). To overcome the drawback of the TE-dependence, several works have used two-dimensional, DW and T2W, experiments enabling the disentanglement of the T2W and the non-T2W model parameters (Collier et al., 2018; Farrher et al., 2020; Gong et al., 2020; Lampinen et al., 2019; Peled et al., 1999; Veraart et al., 2017). The use of two-dimensional experimental protocols such as these has been shown to not only provide TE-independent compartmental signal fractions, but also to offer mitigation to the degeneracy in parameter estimation (Collier et al., 2018; Gong et al., 2020; Jelescu et al., 2016; Veraart et al., 2017). In a recent work, Gong et al. (2020) demonstrated that the extension of conventional NODDI to handle DW and T2W data (i.e. multi-echo (MTE)-NODDI) can be readily achieved by incorporating the compartmental T2-dependence into the model and performing the parameter estimation via a multi-step fitting approach. Nonetheless, MTE-NODDI still has the persisting limitation of the fixed intrinsic diffusivity as it is fundamentally based on conventional NODDI. That being said, preliminary results using MTE-NODDI with fixed d (Farrher et al., 2023) in stroke cases suggest that the compartmental T2 values also differ in ischemic tissue, hence highlighting the need for further investigations.

The primary aim of this study is to assess the benefits and limitations of MTE-NODDI in the investigation of diffusion and T2 properties of ischaemic stroke following middle cerebral artery occlusion (MCAo) in the rat brain. Furthermore, given that the intrinsic diffusivity is expected to be altered in ischaemic tissue (Budde and Frank, 2010; Kamiya et al., 2020; Lampinen et al., 2021; Novikov et al., 2019), our secondary goal is to assess an estimation approach for MTE-NODDI parameters that allows the intrinsic diffusivity to be released whilst mitigating the model degeneracy. The proposed estimation approach differs from the original work by Gong et al. (2020) in three key aspects: i) the intrinsic diffusivity is released, ii) the TE-dependent, conventional NODDI parameters are estimated for all TEs simultaneously, and iii) the intrinsic diffusivity and the orientation dispersion parameter are directly obtained as TE-independent parameters.

This study is organised into two main parts. In the first part, the use of the l_2-norm regularisation in the estimation of MTE-NODDI parameters with released d is investigated, with the optimal regularisation parameter being determined via the L-curve method. The second part of this work is devoted to the investigation of diffusion and T2 properties in rat ischaemic tissue by means of the MTE-NODDI model with released d. In particular, we assess the spatiotemporal evolution of the novel contrasts achieved by releasing d, and by the intra- and extra-neurite relaxation times from the late acute to the chronic phases of stroke. Finally, we discuss the newly estimated MTE-NODDI parameters in light of the current related literature and their biophysical interpretation.

2. Materials and methods

2.1. Background

MTE-NODDI is a multi-compartment model of diffusion and T2 that extends the conventional NODDI (Zhang et al., 2012) to account for differences in the compartmental T2 (Gong et al., 2020). In brief, let us assume that a conventional NODDI protocol has been executed for N_{T2W} different TE values. Then, the DW and T2W signal for the i^{th} TE $(i = 1, \ldots, N_{T2W})$ can be written as:

$$S_i(b, \mathbf{q}; \boldsymbol{\theta}_i) = S_{0,i}\left[f_{iso,i}S_{iso}(b) + \left(1 - f_{iso,i}\right)\left(f_{in,i}S_{in}(b, \mathbf{q}; \kappa, d) + \left(1 - f_{in,i}\right)S_{en}\left(b, \mathbf{q}; f_{in,i}, \kappa, d\right)\right)\right], \quad (1)$$

where b is the b-value and $\mathbf{q}$ is the direction of the diffusion-encoding field gradient. The compartment-specific signals are: $S_{iso} = e^{-bd_{iso}}$, with $d_{iso} = 3\ \mu m^2/ms$; $S_{en} = e^{-b\mathbf{q}^T\left(\int W(\mathbf{n};\boldsymbol{\mu},\kappa)\mathbf{D}_i(\mathbf{n})d\mathbf{n}\right)\mathbf{q}}$, where $\mathbf{D}_i(\mathbf{n}) = d\left[f_{in,i}\mathbf{n}\mathbf{n}^T + \left(1 - f_{in,i}\right)\mathbf{I}\right]$ is the extra-neurite diffusion tensor, d is the intrinsic diffusivity, and $\mathbf{I}$ the 3×3 identity matrix; and $S_{in} = \int W(\mathbf{n};\boldsymbol{\mu}, \kappa)e^{-bd\left(\mathbf{q}^T\mathbf{n}\right)^2}d\mathbf{n}$. In the equations for S_{en} and S_{in}, the integral is performed over the unit sphere and $W(\mathbf{n};\boldsymbol{\mu}, \kappa)$ denotes the Watson distribution for a gradient direction $\mathbf{n}$, given the concentration parameter $\kappa \in [0, \infty)$ –which is additionally related to the orientation dispersion index according to $ODI = 2\arctan(1/\kappa)/\pi \in [0, 1]$ (Zhang et al., 2012)– and the mean orientation vector, $\boldsymbol{\mu}$, which can be set equal to the principal eigenvector of the standard diffusion tensor (Daducci et al., 2015). The vector $\boldsymbol{\theta}_i = \left\{S_{0,i}, f_{iso,i}, f_{in,i}, \kappa, d\right\}$ contains the model parameters, where the TE-dependent parameters are the non-DW signals, $S_{0,i}$, and isotropic and intra-neurite signal fractions, $f_{iso,i}$ and $f_{in,i}$. The TE-independent parameters are κ and d. In conventional NODDI, d is fixed to 1.7 $\mu m^2/ms$ for the whole brain (Zhang et al., 2012). However, here, it is included in the definition of $\boldsymbol{\theta}_i$ because we aim to release it.

The TE-dependent compartmental fractions, $f_{in,i}$ and $f_{iso,i}$, relate to their TE-independent counterparts, $f_{in,0}$ and $f_{iso,0}$, according to (Gong et al., 2020):

$$f_{in,i} = \frac{f_{in,0}e^{TE_i\Delta R_{2,en-in}}}{f_{in,0}e^{TE_i\Delta R_{2,en-in}} + \left(1 - f_{in,0}\right)}$$

and

$$f_{iso,i} = \frac{f_{iso,0}e^{TE_i\Delta R_{2,in-iso}}}{f_{iso,0}e^{TE_i\Delta R_{2,in-iso}} + \left(1 - f_{iso,0}\right)f_{in,0}/f_{in,i}}, \quad (2)$$

where $\Delta R_{2,en-in} = 1/T_{2,en} - 1/T_{2,in}$ and $\Delta R_{2,in-iso} = 1/T_{2,in} - 1/T_{2,iso}$, and $T_{2,in}$, $T_{2,en}$ and $T_{2,iso}$ denote the intra-neurite, extra-neurite and isotropic T2 times, and TE_i is the i^{th} echo time.

The MTE-NODDI method as proposed by Gong et al. (2020), aims to estimate the parameters $f_{iso,0}$, $f_{in,0}$, ODI, $T_{2,in}$ and $T_{2,en}$ in a multi-step manner, which is summarised as follows:

i. Estimate $f_{in,i}$, $f_{iso,i}$ and ODI independently for each DW dataset linked to each TE (Eq. (1)). Note that given its TE-independence, ODI is evaluated as the arithmetic mean of the ODI values estimated for all TEs;
ii. estimate $\Delta R_{2,en-in}$ and $f_{in,0}$ from the slope and intercept of

$$\ln\frac{f_{in,i}}{1 - f_{in,i}} = TE_i\Delta R_{2,en-in} + \ln\frac{f_{in,0}}{1 - f_{in,0}} \quad (3)$$

iii. estimate $\Delta R_{2,in-iso}$ and $f_{iso,0}$ from the slope and intercept of

$$\ln\frac{f_{in,0}f_{iso,i}}{f_{in,i}\left(1 - f_{iso,i}\right)} = TE_i\Delta R_{2,in-iso} + \ln\frac{f_{iso,0}}{1 - f_{iso,0}} \quad (4)$$

iv. estimate $T_{2,in}$ from the slope of

$$\ln\left[S_i(b = 0)f_{in,i}\left(1 - f_{iso,i}\right)\right] = -\frac{TE_i}{T_{2,in}} + \ln S_{in,0} \quad (5)$$

v. calculate $T_{2,en}$ based on the definition of $\Delta R_{2,en-in}$.

Notice that $T_{2,iso}$ may also be estimated (Gong et al., 2020). However, due to the experimental design utilised in the present study, its estimation is highly unstable, and it is therefore excluded from further discussions.

2.2. Animals

All animal procedures were as described in (Farrher et al., 2021) and were approved by the Institutional Animal Care and Use Committee at the National Health Research Institutes (Taiwan). Adult male Sprague-Dawley rats (BioLASCO, Taipei, Taiwan), weighing 300–400 g, were anaesthetised with chloral hydrate (0.4 g/kg, intraperitoneal injection, Sigma-Aldrich). The right middle cerebral artery (MCA) was ligated with a 10–0 suture (N-2540, Monosof TM Covidien, Minneapolis, MN, USA), and common carotid arteries were clamped bilaterally using non-traumatic arterial clips, together efficiently reducing > 80 % blood flow in the MCA. As a result, focal ischaemia in the cerebral cortex is induced, as described previously (Chen et al., 1986; Liu et al., 2011; Yu et al., 2020). The ligature and clamps were removed after 90 min to generate reperfusion injury. Core body temperature was monitored and maintained at 37 °C by a heating pad during surgery. After recovery from the anaesthesia, the body temperature was maintained at 37 °C using a temperature-controlled incubator. A custom-made rat head holder and a circulating heated water bath were used. All rats were anaesthetised with 1–2 % isoflurane in oxygen during the MRI scans. Respiration was kept at 40–50 breaths per minute, and body temperature was maintained at 37 °C. This was monitored using a small animal physiological monitoring and control unit (SA Instruments, Stony Brook, NY).

Two sets of animals were measured, each set having different time points. For the first set, rats were subjected to longitudinal MRI experiments, including measurements prior to MCAo (5 rats) and on days 1 (3), 2 (3) and 23 (4) after MCAo. For the second set, the MRI experiments were performed prior to MCAo (6 rats) and on days 1 (4), 3 (4), 4 (4), 5 (4), 6 (4), 7 (4) and 10 (4).

2.3. MRI experiments

The experimental protocol was followed as described elsewhere (Farrher et al., 2021). MRI experiments were performed on a home-integrated, translational 3T MRI scanner equipped with an ultra-high-strength gradient system (maximum strength of 675 mT/m) (Cho et al., 2019). A custom-built, single-loop transmit/receive surface coil was utilised. A Stejskal-Tanner segmented echo-planar imaging

pulse sequence was employed with the following parameters: repetition time, TR = 9 s; echo time, TE = 50, 100 ms; *b*-values (directions) = 0 (8), 0.5 (12), 1.0 (26) and 2.0 (40) ms/μm^2; diffusion gradient separation and duration, Δ = 24 ms and δ = 3 ms; field of view, FOV = 25 × 25 mm^2; matrix-size = 96 × 96; voxel-size = 0.26 × 0.26 × 1 mm^3; 20 slices; phase-encoding direction anterior-to-posterior. One extra volume with opposite phase-encoding was acquired for the correction of susceptibility-induced distortions. A turbo spin-echo sequence was used to acquire T2W structural images. The protocol parameters were: TR = 4 s; TE = 68 ms; 6 repetitions; FOV = 25 × 25 mm^2; matrix-size = 192 × 192; voxel-size = 0.13 × 0.13 × 1 mm^3; 20 slices.

2.4. Estimation of MTE-NODDI parameters with released *d*

Prior to the estimation of the MTE-NODDI parameters, the data were denoised as described in (Veraart et al., 2016) and implemented in MRtrix (Tournier et al., 2019). Correction of the positive signal bias due to its Rician nature was performed following the method by Gudbjartsson and Patz (1995), using the background noise standard deviation obtained at the denoising step (Veraart et al., 2017). Gibbs-ringing artefact correction was performed using the approach by Kellner et al. (2016), implemented in MRtrix. Susceptibility-induced and eddy-current distortions were corrected using `topup` and `eddy`, provided by FSL (Andersson et al., 2003; Smith et al., 2004). The remaining processing was completed using in-house Matlab scripts (Matlab 2022b, The MathWorks, MA, USA).

The approach proposed for the estimation of MTE-NODDI parameters in this work refers to step i) in subSection 2.1, whereas steps ii)-v) are executed as originally proposed by Gong et al. (2020). In our approach, instead of fitting the NODDI signal equation (Eq. (1)) to each DW dataset independently, the TE-dependent parameters are simultaneously estimated for all DW datasets, with κ and d as shared, TE-independent parameters. Hence, the cost function to be minimised is written as

$$F = \sum_{i=1}^{N_{T2W}} \sum_{j=1}^{N_{DW}} \left[S_i\left(b_j, \mathbf{q}_j; \boldsymbol{\theta}_i\right) - M_{ij} \right]^2 + \lambda \| \boldsymbol{\Omega} \|_2^2, \quad (6)$$

where N_{DW} is the number of DW volumes per TE, M_{ij} are the signals measured at echo time TE_i and diffusion weighting settings $\left(b_j, \mathbf{q}_j\right)$ and $\boldsymbol{\Omega} = \left\{ S_{0,1}, \cdots, S_{0,N_{T2W}}, f_{iso,1}, \cdots, f_{iso,N_{T2W}}, f_{in,1}, \cdots, f_{in,N_{T2W}}, \kappa, d \right\}$ is the vector containing the $3N_{T2W} + 2$ free parameters. The term $\lambda \| \boldsymbol{\Omega} \|_2^2$ denotes the l_2-norm regularisation, with λ being the regularisation parameter. For the experimental settings in this work, we have $N_{T2W} = 2$ and therefore $\boldsymbol{\Omega} = \left\{ S_{0,1}, S_{0,2}, f_{iso,1}, f_{iso,2}, f_{in,1}, f_{in,2}, \kappa, d \right\}$. In order to handle the multiple TE datasets, the NODDI signal model was implemented in-house using Matlab, whereas the function `WatsonSHCoeff` was borrowed from the NODDI Matlab Toolbox (v1.04, http://mig.cs.ucl.ac.uk/index.php?n=Tutorial.NODDImatlab) (Zhang et al., 2012). Minimisation of Eq. (6) was performed using `fmincon`, available in Matlab.

The advantage of fitting all TE datasets simultaneously is two-fold. Firstly, the independence of κ and d on TE can be directly imposed during estimation (Eq. (6)), and the need to evaluate *ODI* and d as an arithmetic mean is avoided. Secondly, the following constraints can be imposed during minimisation of F: a) $S_{0,i+1} < S_{0,i}$ (as a result of the overall signal transverse relaxation) and b) $f_{iso,i} < f_{iso,i+1}$, which stems from the fact that $T_{2,iso} \gg T_{2,in}, T_{2,en}$ (Benjamini and Basser, 2017). Conversely, we refrain from imposing $f_{in,i} < f_{in,i+1}$ because although this condition holds true for WM, the case for GM has not yet been established conclusively (Benjamini and Basser, 2017; Dortch et al., 2010; Veraart et al., 2017; Whittall et al., 1997). Other box constraints are: $f_{iso,i}$, $f_{in,i} \in [0, 1]$; $\kappa \in [0, 64]$ (Jelescu et al., 2016); $d \in [0.3, 3.1]$ μm^2/ms (Guerrero et al., 2019). Note also that, given that the global signal depends on several hardware-related factors, such as coil sensitivity, loading and receiver gain, among others, the signals M_{ij} were, before the minimisation of Eq. (6), normalised by the corresponding non-DW and non-T2W signal, S_0, as estimated using conventional DTI with explicit account for T2 signal attenuation (DTIT$_2$) (Fan and Does, 2008; Farrher et al., 2021; Lampinen et al., 2023). Hence, the global signal intensity, and consequently the regularisation parameter, is comparable across animals. Moreover, the additional box constraint $S_{0,i} \in [0, 1]$ can be set. The equivalence between the original and the method proposed here for step i) in the estimation of MTE-NODDI parameters is shown in supplementary material S.1. The initial guess for the model parameters was determined based on an analysis of the solution landscape (described and discussed in supplementary material S.2) and set to: $S_{0,1} = M_{1,1}$, $S_{0,2} = M_{2,1}$, $f_{iso,1} = 0.05$, $f_{iso,2} = 0.1$, $f_{in,1} = 0.4$, $f_{in,2} = 0.6$ and $d = 1$ μm^2/ms. For the case of κ, the fitting was performed for four different initial values: $\kappa = 0.1$, 1, 3 and 7, and the solution with the lowest value of F was taken as the "best fit" (Jelescu et al., 2016).

2.5. Evaluation of the regularisation parameter

To determine the optimal regularisation parameter, the L-curve criterion was employed (Hansen, 2000). This method involves plotting the norm of the regularised solution (second term in Eq. (6)) against the norm of the residuals (first term in Eq. (6)) in a logarithmic plot. The value of λ can then be found at the point at which the L-curve has the maximum curvature. Thus, the corner of maximum curvature provides a value of λ, for which there is a trade-off between both terms.

To evaluate the L-curve, minimisation of Eq. (6) was first performed voxel-wise for 30 values of $\lambda \in \left[5 \times 10^{-6}, 5 \times 10^{-3}\right]$ for three slices (Bregma 0.48, −0.48 and −1.44) in a single animal. Secondly, the curvature, c, was evaluated voxel-wise for all values of λ with the help of the function `LineCurvature2D`, available for Matlab (Kroon, 2011), using the pair of input variables $x = \ln \| \boldsymbol{\Omega} \|_2^2$ and $y = \ln \sum_{i=1}^{N_{T2W}} \sum_{j=1}^{N_{DW}} \left[S_i\left(b_j, \mathbf{q}_j; \boldsymbol{\theta}_i\right) - M_{ij} \right]^2$ (Hansen, 2000). The maximum of the curvature was then found voxel-wise via a linear search, and a map of the optimal λ was created. Finally, with the purpose of obtaining a single value for the whole brain, a histogram of the optimal λ map was created and the value of λ for the whole brain was chosen as its peak value.

2.6. Data simulation

The precision and accuracy of the MTE-NODDI parameters were assessed via simulation for three tissue types: healthy GM and WM, and ischaemic GM. The experimental protocol was the same as in the in vivo experiments. The ground truth MTE-NODDI parameters were taken from 50 random voxels in each tissue type. Three estimation approaches were considered: the conventional approach employing fixed diffusivity (=1.7 μm^2/ms), and the unregularised ($\lambda = 0$) and regularised ($\lambda = 6 \times 10^{-4}$) cases with released diffusivity. Each of the 50 voxels was simulated for 100 Rician noise realisations with SNR = 50, corresponding to the typical values observed in our experiments. No data preprocessing was performed for the simulated data as in Gong et al. (2020). Subsequently, the following statistical metrics were computed: the absolute bias, $b = |E[A] - A_0|$, where A denotes one of the MTE-NODDI parameters, A_0 its corresponding ground truth, and $E[A]$ the expectation value across the noise realisations; the standard deviation, $s = E\left[(A - E[A])^2\right]^{1/2}$, and the mean square error (MSE), $m = b^2 + s^2$ (Sijbers and den Dekker, 2004).

2.7. Statistical analysis

Following previous works (Farrher et al., 2021; Lin et al., 2002;

Wagner et al., 2012), regions-of-interest (ROIs) covering the cortex on the ipsilateral and contralateral hemispheres were manually drawn on slices 1 and 2 (Bregma 0.48 mm and −0.48 mm, respectively (Paxinos and Watson, 2004)), using the maps of fractional anisotropy (FA) from $DTIT_2$ as a visual guide. The mean and standard deviation of all MTE-NODDI parameters were calculated separately for each animal and each time point. In the following, the mean and standard deviation of a parameter A over a given ROI will be indicated as $\overline{A}$ and σ_A, respectively. Additionally, the mean, $\langle\overline{A}\rangle$, and the standard error of the mean (SEM) over animals were computed and plotted against the time after MCAo. Furthermore, the average of the standard deviation across animals, $\langle\sigma_A\rangle$, was also evaluated in order to investigate the temporal evolution of the biologically-induced ROI heterogeneity (Wagner et al., 2012). A two-tailed paired t-test was utilised to test for significant differences between the ipsilateral and contralateral ROIs for each MTE-NODDI parameter at each time point. Similarly, a two-tailed paired t-test was also employed to investigate the difference between intra- and extra-neurite T2 times for each time point.

2.8. Group-wise templates of MTE-NODDI parameters

The spatiotemporal evolution of MTE-NODDI parameters was further inspected via the construction of a group-wise template for each time point. To this end, a multi-variate template was created with the help of the script `antsMultivariateTemplateConstruction2.sh` available in ANTs (Avants et al., 2011) using the maps of FA, axial (AD) and radial (RD) diffusivities, and T_2 from $DTIT_2$ as input (Farrher et al., 2021). Subsequently, the affine transformation (firstly) and the warp field (secondly) were applied to all MTE-NODDI maps of each animal. Finally, the voxel-wise mean was calculated for each time point. The mean values of each MTE-NODDI parameter were calculated prior to stroke onset over two ROIs drawn at the cortices and one ROI comprising the corpus callosum and the external capsule, for the sake of comparison with values previously reported in the literature. Both ROIs were drawn over slices 1 and 2. However, we refrain from performing a detailed analysis of MTE-NODDI parameters for all anatomical regions within the studied slices because of the limited resolution of our imaging protocol as well as the low SNR values in the lower part of the brain.

3. Results

The procedure for the evaluation of λ in a rat brain is summarised in Fig. 1a-c. Fig. 1a shows the typical L-curve obtained from a single voxel. The inset shows the calculated curvature, c, for every point in the L-curve, with the maximum value highlighted by the red dot. Fig. 1b demonstrates the reconstructed map of the optimal λ for a slice, and Fig. 1c shows the corresponding histogram taken over three slices. The peak of the histogram is located at $\lambda = 6 \times 10^{-4}$, which was used for all datasets in the remainder of this work. Plots in Fig. 1d and e display the map and histogram of the SNR values, respectively, and Fig. 1f demonstrates the two-dimensional histogram of λ versus SNR. The Spearman's rank correlation coefficient resulted in $r = -0.46$ ($p < 10^{-10}$).

Fig. 2 shows the estimated maps of the parameters in the vector $\boldsymbol{\Omega}$, i.e. the TE-dependent isotropic (first column) and intra-neurite (second column) fractions, the concentration parameter (third column) and the intrinsic diffusivity (fourth column) without (i.e. $\lambda = 0$ (a)) and with regularisation ($\lambda = 6 \times 10^{-4}$ (b)). The maps in Fig. 2a show that the estimation without regularisation displays, across voxels from similar anatomical structures, changes much larger than those expected from biological variability. This feature is particularly prominent in the map of κ, which displays two distinct sets of solutions: one set characterised by $\kappa \lesssim 10$ (genuine solution) and another where $\kappa \approx 64$ (spurious

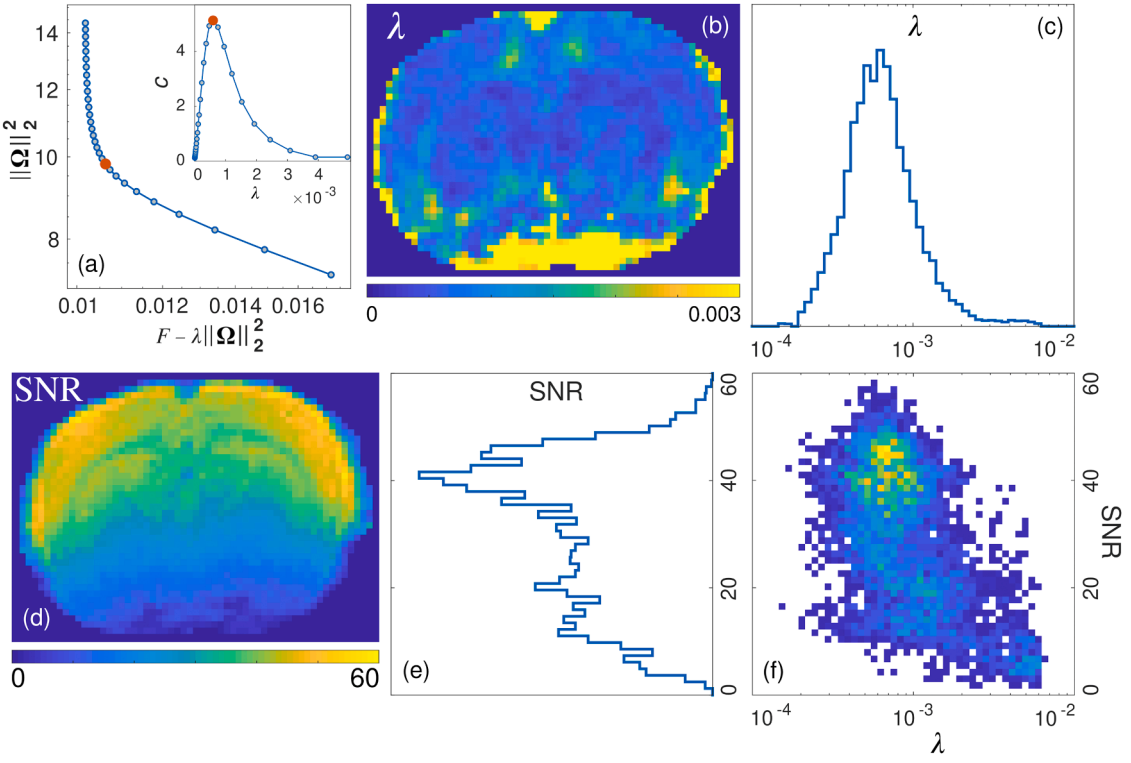

Fig. 1. Application of the L-curve method for the evaluation of the optimal regularisation parameter. (a) L-curve for a representative voxel (inset: point-by-point curvature of the L-curve for all λ values). The red dot denotes the point of maximum curvature for this exemplary voxel. (b) A map of the optimal λ for a representative slice in animal 1. (c) The histogram of the optimal λ taken over 3 slices. The peak of the histogram, located at $\lambda = 6 \times 10^{-4}$, is taken as the whole-brain optimal regularisation parameter. (d) A map of the SNR values, and (e) the corresponding histogram. (f) Two-dimensional histogram depicting the correlation of λ vs. SNR. The Spearman's rank correlation coefficient resulted $r = -0.46$ ($p < 10^{-10}$). Notice that, due to the discrete nature of the initial λ range, the map of λ was smoothed using a discretised spline smoothing implemented in the Matlab function `smoothn` (Garcia, 2010), prior to the histogram evaluation.

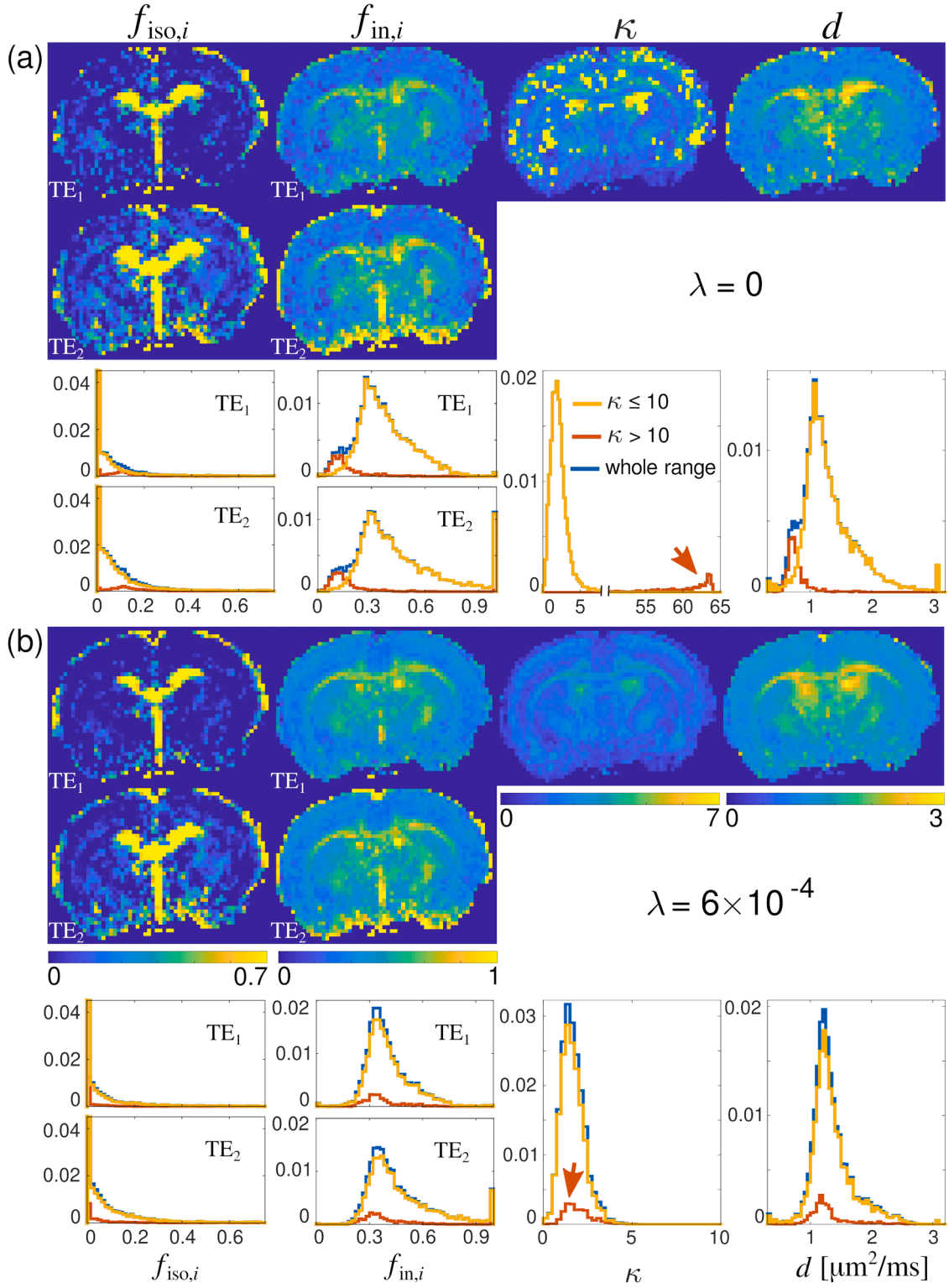

Fig. 2. Comparison of the TE-dependent ($f_{iso,i}$ and $f_{in,i}$) and TE-independent (κ and d [μm^2/ms]) parameters for the case where the estimation was performed without regularisation (a), i.e. $\lambda = 0$, versus the case where the regularisation was applied (b), i.e. $\lambda = 6 \times 10^{-4}$. The maps are shown in the top panels, whereas the corresponding histograms, taken over 3 slices are shown in the bottom panels. The maps of κ for the unregularised case (a) were used to create a mask dividing the voxels into sets of genuine ($\kappa \leq 10$, yellow lines) and spurious ($\kappa > 10$, red lines and red arrow) solutions. The blue lines refer to the whole-slice histograms. The same mask was utilised to study the behaviour of both sets of voxels for the regularised case (b).

solution). Note that the latter κ value simply represents the upper boundary typically used in conventional NODDI. The former observation is more evidently revealed by the histogram of each parameter, shown at the bottom of panel (a). Here, the yellow lines correspond to the voxels where the genuine solution was achieved, whereas the red lines refer to the spurious solution. Besides being characterised by large κ values (red arrow in Fig. 2a), the spurious solution displays distinct peaks at lower values for $f_{in,i}$ and d. For a more detailed analysis of the

solution landscape, the reader is referred to supplementary material S.2. The large κ values for the spurious voxels suggest that the l_2-norm regularisation could be a suitable approach to suppress the solution characterised by large κ values. Indeed, no spurious solutions can be observed in the maps shown in Fig. 2b, nor in the corresponding histograms, where the peaks related to the voxels that showed spurious solutions when no regularisation was used (red lines in (a)), appear within the range of genuine values when the regularisation was applied (b).

Fig. 3 shows a comparison of the maps of conventional MTE-NODDI, i.e. $d = 1.7$ μm^2/ms (top row) and its version with released d (second row) for a rat brain one day after stroke. A post-stroke brain was selected for this comparison because it was anticipated that the benefit of releasing d would be much clearer in ischaemic tissue (Farrher et al., 2023). For MTE-NODDI with fixed d at the ischaemic tissue, $f_{\text{in},0}$ tends to reach values equal unity which, in turn, translate into artefacts in $T_{2,\text{en}}$ as a consequence of its estimation method (Eq. (3)). Conversely, when d is released, the values of $f_{\text{in},0}$ at the ipsilateral cortex are < 1 and, as a consequence, the estimation of $T_{2,\text{en}}$ depicts no artefacts. Note that the estimation of both T2 values appears to be highly unstable in low-SNR voxels (lower part of the brain) in both cases, implying that the release of d is not the main cause for this instability. Similarly, while the conventional $f_{\text{iso},0}$ shows no visible differences between the ipsilateral and contralateral sides, its version with released d unmistakably reveals an increase in the isotropic water fraction in the whole ischaemic area. Moreover, the newly obtained d map not only shows a significant dispersion of values between different healthy tissue types, but also displays a clear reduction in the ischaemic tissue compared to the contralateral part. In terms of $T_{2,\text{in}}$, no visual differences between the estimation approaches can be observed in either the maps or the histograms.

Fig. 4 demonstrates the scatter plots of the simulated MTE-NODDI parameters (ordinates) for WM (a-f), healthy GM (g-l), and ischaemic GM (m-r) versus their respective ground truth values (abscissas). Blue and red dots refer to the unregularised and regularised cases, respectively. The larger, cyan (unregularised case) and orange (regularised case) circles display the mean values taken across the noise realisations for each of the 50 simulated voxels. In general, for the three tissue types, the regularised MTE-NODDI parameters display both lower bias (i.e. dots closer to the identity line depicted by the dashed, grey line) and standard deviation (i.e. lower dots spread). As expected, the parameter most notably affected by the regularisation is κ.

Fig. 5 displays the absolute bias (a-f), the standard deviation (g-l) and the MSE (m-r) of MTE-NODDI parameters for each simulated tissue type, for the unregularised (blue) and regularised cases (red), as well as for the conventional case with fixed d (grey). The height of each bar and error bars denote the mean and standard deviation of each metric taken across the 50 simulated voxels. The three statistical metrics of all parameters for the regularised case are generally reduced, compared to that of the unregularised case. The presence of the solution characterised by large κ values for the unregularised case is demonstrated by its large bias and standard deviation (blue bars in c, i and o).

Figs. 6 and 7 show the spatiotemporal evolution of MTE-NODDI parameter maps for a rat in group 1 and a rat in group 2 (one slice, Bregma 0.48), respectively, referred to as rat 1 (Fig. 6) and rat 2 (Fig. 7) from here onwards. The maps of conventional mean diffusivity (MD), FA and T_2 estimated using the DTIT$_2$ method and the high-resolution T2W images are additionally shown for visual reference. All diffusion- and microstructure-related maps are depicted in the topmost panels, whereas the relaxation-time-related parameters are depicted in the middle panels. In general, all MTE-NODDI maps show not only different degrees of contrast between the ischaemic and the contralateral tissue but are also heterogeneous and heterochronous.

Besides the typical patterns of increased isotropic fraction at the tissue-CSF interface (Collier et al., 2018; Farrher et al., 2021, 2020; Pasternak et al., 2009), $f_{\text{iso},0}$ shows an increment in the ipsilateral cortex one day after stroke, with further increments on day two (Figs. 6 and 7). From day three onwards, the distribution of $f_{\text{iso},0}$ over the ischaemic cortex becomes more heterogeneous (Fig. 7), with the core of the ischaemic zone displaying a different behaviour compared to the border zone. In contrast, the intra-neurite fraction shows only a slight increase one day after stroke but retracts to visually normal values from day three onwards. Finally, $f_{\text{in},0}$ tends to reduce further below normal values between days 10 and 23. The values of *ODI* display a large increment on day one after stroke, which remains elevated until day 23 when the values appear to downtrend (Fig. 6). The value of d is homogeneously reduced on days one and two after stroke (Figs. 6 and 7). From day three onwards, it remains abnormally low at the core zone but tends to rise above normal values at the inner border zone (Fig. 7). This feature is particularly difficult to perceive, because its adjacent external capsule

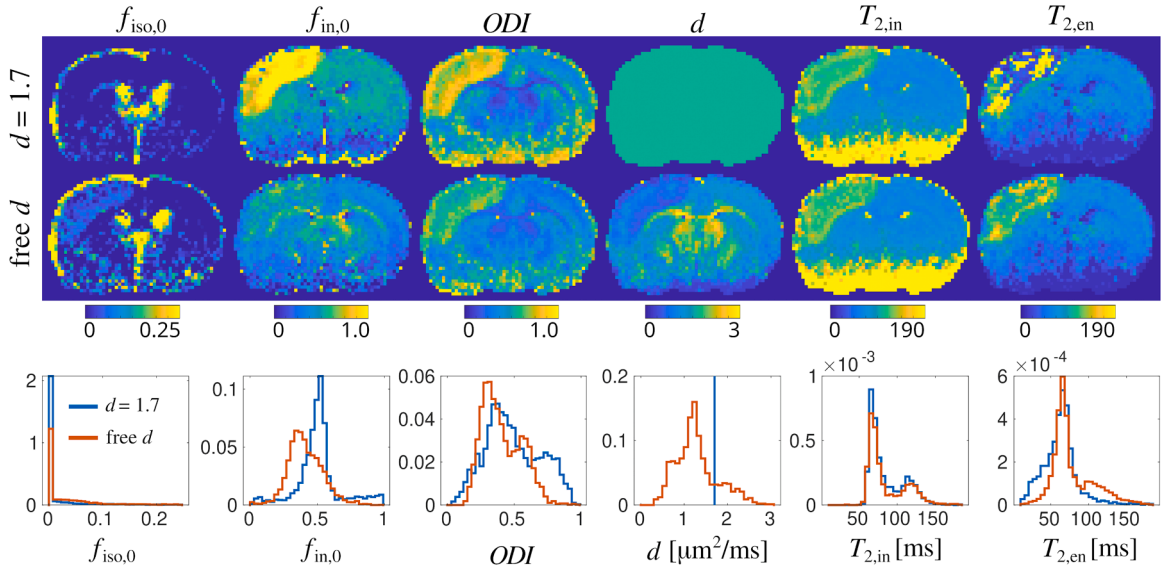

Fig. 3. A comparison of MTE-NODDI maps, between the conventional approach where the intrinsic diffusivity is set to $d = 1.7$ μm^2/ms (top row), and the approach proposed in this work, where d is released, with regularisation parameter $\lambda = 6 \times 10^{-4}$ (middle row). The corresponding histograms are shown in the bottom row. Notice that an animal was chosen on day 1 post-stroke in order to emphasise the strong limitations of conventional MTE-NODDI with fixed d in voxels in ischaemic tissue.

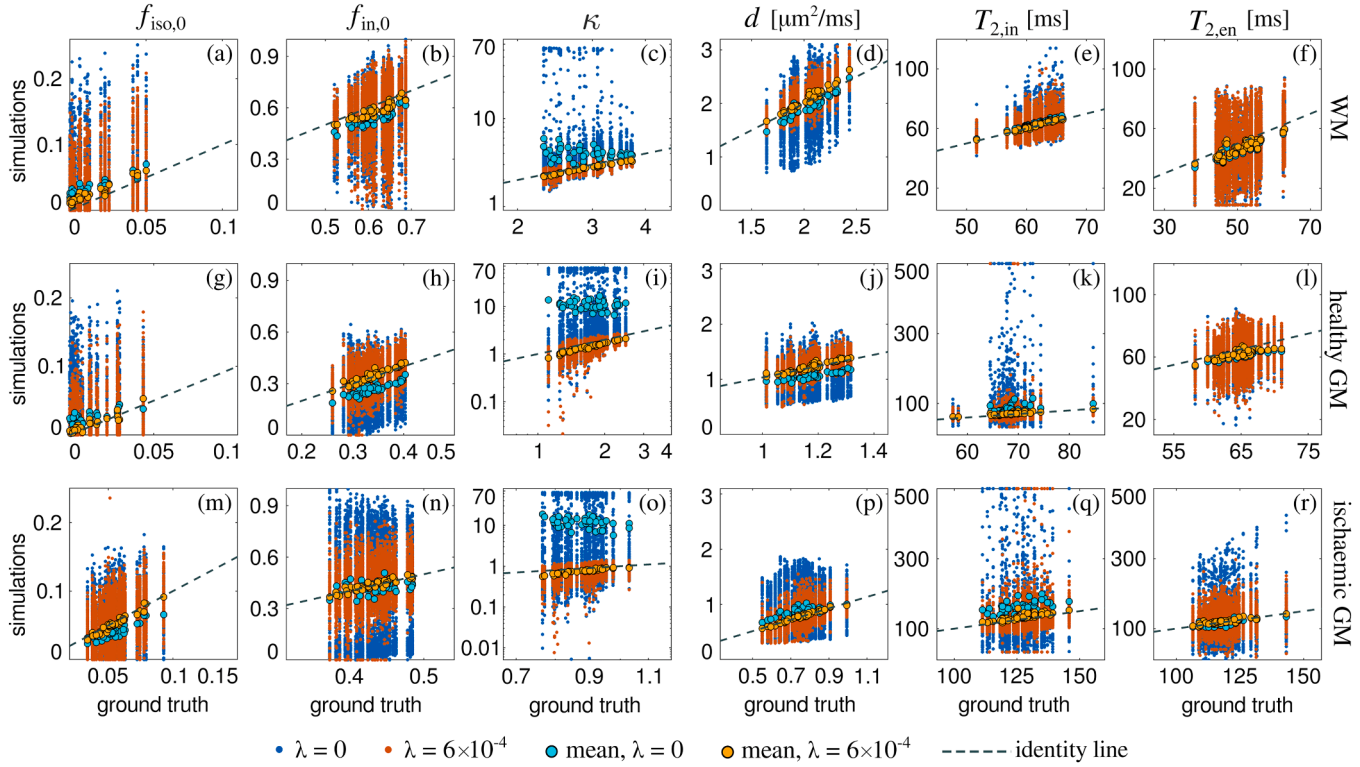

Fig. 4. Scatter plots of the simulated MTE-NODDI parameters (ordinates) for WM (a-f), healthy GM (g-l), ischaemic GM (m-r) versus their respective ground truth values (abscissas). Blue and red dots denote the unregularised and regularised cases, respectively. The larger, cyan (unregularised case) and orange (regularised case) dots display the mean values taken across the noise realisations for each of the 50 simulated voxels. The dashed, grey lines denote the identity line. Notice the logarithmic scales in the plots of κ (c, i, o), set for the sake of better visualisation.

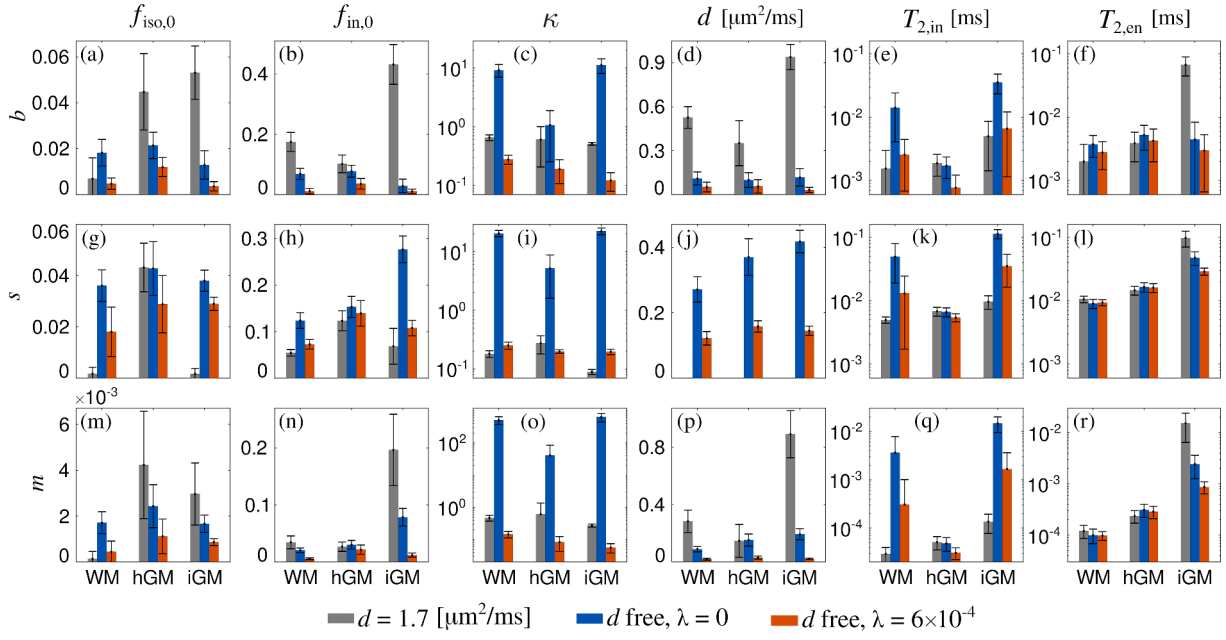

Fig. 5. Plots of the absolute bias (a-f), the standard deviation (g-l) and the MSE (m-r) of the MTE-NODDI parameters for each simulated tissue type, for the unregularised (blue) and regularised cases (red), as well as for the conventional case with fixed d (grey). The height of each bar and the error bars denote the mean and standard deviation, respectively, of each metric taken across the 50 simulated voxels. Note that the ordinate axes for metrics κ, $T_{2,in}$ and $T_{2,en}$ were set to logarithmic for the sake of better visualisation. hGM: healthy GM; iGM: ischaemic GM.

shows similar d values. However, if MD and FA are used as a visual guide, the elevated d values at the inner border zone become more evident, as seen by the different spatial thicknesses of that region at the different maps (magenta arrows in Fig. 7). Finally, by day 23, the values of d are well above normal values.

The relaxation times $T_{2,in}$ and $T_{2,en}$ both rose on day one after stroke,

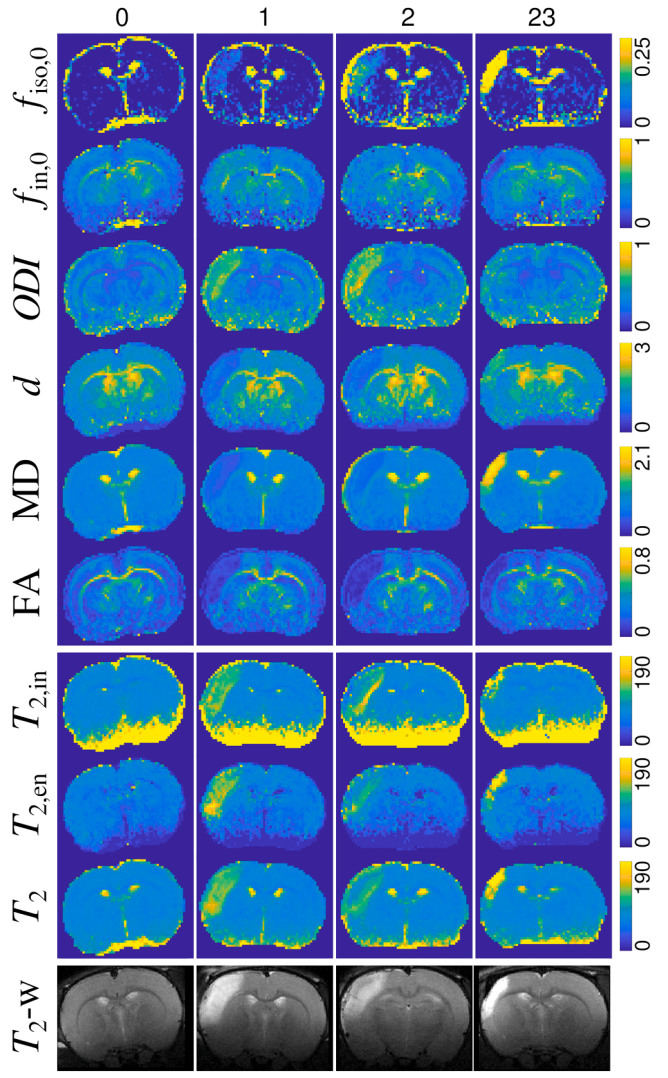

Fig. 6. Spatiotemporal evolution of MTE-NODDI parameter maps for a rat in group 1 (Bregma 0.48) along with MD, FA and T_2 maps from the conventional DTIT$_2$ method. The top panel depicts the microstructure- and diffusion-related maps, the middle panel the relaxation-related maps and the bottom panel the high-resolution T2W images. The units for diffusion maps are μm^2/ms, while the units for relaxation times are ms.

although different degrees of heterogeneity between rats 1 and 2 can be observed. Starting on day two, $T_{2,in}$ and $T_{2,en}$ show a spatiotemporal evolution which is different between the core and the inner border zone. At the core area, both relaxation times tend to renormalise between days one and six but do not reach the normal contralateral values. From day seven onwards, the values of $T_{2,in}$ and $T_{2,en}$ at the core zone start increasing again. Conversely, both relaxation times at the inner border zone tend to increase starting on day two and reach a maximum at around days four and five. Between days six and seven, $T_{2,in}$ decreases, whereas $T_{2,en}$ remains elevated. Finally, at days 10 and 23, both relaxation times show a lower spatial heterogeneity with larger-than-normal values.

Fig. 8 shows the template maps of all the MTE-NODDI parameters obtained by averaging the maps from all animals within every time point (Bregma 0.48). In general, all template maps resemble analogous spatiotemporal behaviour as the MTE-NODDI maps for single rats. Interestingly, the heterogeneity patterns of $T_{2,in}$ and $T_{2,en}$ during all phases of stroke appear more similar to that of $f_{iso,0}$, where the ischaemic core evolves differently compared to the border zone. In contrast, the parameters $f_{in,0}$ and *ODI* show a less heterogeneous distribution throughout the investigated time frame. As a reference for the healthy tissue, the mean values calculated for the ROIs at the cortex before stroke were: $f_{iso,0} = (0.006 \pm 0.009)$; $f_{in,0} = (0.33 \pm 0.04)$; $ODI = (0.37 \pm 0.07)$; $d = (1.17 \pm 0.08)$ μm^2/ms; $T_{2,in} = (68 \pm 3)$ ms and $T_{2,en} = (64 \pm 2)$ ms. For the WM ROI: $f_{iso,0} = (0.009 \pm 0.010)$; $f_{in,0} = (0.61 \pm 0.05)$; $ODI = (0.22 \pm 0.03)$; $d = (2.04 \pm 0.20)$ μm^2/ms; $T_{2,in} = (62 \pm 3)$ ms and $T_{2,en} = (50 \pm 6)$ ms.

Fig. 9 illustrates the histograms of the MTE-NODDI parameters taken over two slices in a rat from group 1 before stroke (Fig. 9a) and at days one (Fig. 9b) and 23 (Fig. 9c) after stroke as examples. The histograms were taken over whole slices (blue) and over ROIs covering the ipsilateral (red) and contralateral (yellow) cortices. All parameter maps before stroke show a unimodal distribution. Conversely, all parameters show a bimodal distribution at day one after stroke, where the peak related to the ischaemic cortex is shifted towards larger values for $f_{iso,0}$, $f_{in,0}$, *ODI*, $T_{2,in}$ and $T_{2,en}$ and towards lower values for *d*, compared to the contralateral cortex. On day 23 after stroke, all parameters again show a unimodal distribution, except for $f_{iso,0}$, which exhibits a broad peak shifted towards values much larger than those at the contralateral side. Another exception is *d*, which depicts a shoulder-like shape towards values above normal.

The scatter plots shown in Fig. 9a for two whole slices before stroke (blue), demonstrate that all MTE-NODDI parameters have different degrees of correlation with *d* (see Table 1 for the Spearman's rank analysis). Before and one day after stroke, $f_{iso,0}$, *ODI*, $T_{2,in}$ and $T_{2,en}$ correlate negatively with *d*, whereas for $f_{in,0}$ that correlation is positive. At day 23, the behaviour remains the same, except for $f_{iso,0}$, which is positively correlated with *d*. For the ROIs drawn in the contralateral cortex (yellow), only $f_{in,0}$ and *ODI* retain the same significant correlation as seen in the analysis of whole slices. At the ipsilateral cortex instead (red), we observe a significant, negative correlation of $f_{iso,0}$ and *ODI*, and a positive correlation of $f_{in,0}$ and $T_{2,in}$ with *d* on day one after stroke. Finally, at day 23 after stroke, the correlations of $f_{iso,0}$, $T_{2,in}$ and $T_{2,en}$ turn significantly positive, whereas the correlation of $f_{in,0}$ and *ODI* with *d* results negative.

The group-based ROI analysis of the temporal evolution of the MTE-NODDI parameters is presented in Fig. 10. The average across animals for both within-ROI mean (Fig. 10a-e) and standard deviation (Fig. 10f-j) are shown, along with the error bars indicating the SEM. In general, all parameters at the ipsilateral cortex show significant differences compared to the contralateral cortex. Moreover, as demonstrated by the corresponding standard deviation, the temporal evolution of all parameters shows different degrees of spatial heterogeneity.

4. Discussion

To the best of our knowledge, this study is the first to apply MTE-NODDI to investigate the spatiotemporal evolution of diffusion and relaxation properties in ischaemic brain tissue following MCAo in rats. The study additionally aimed to address a key limitation of MTE-NODDI, which requires the intrinsic diffusivity to be fixed at a single, brain-wide value in order to mitigate the model degeneracy. In the following, the parameters *d* and *ODI* will be discussed in light of the current literature, irrespective of whether they were estimated using NODDI or MTE-NODDI, as they are TE-independent. In contrast, the distinction between NODDI and MTE-NODDI will be made when discussing TE-dependent parameters.

4.1. MTE-NODDI parameter estimation with released d

We have observed that simply releasing *d* leads to a degeneracy in the solution landscape, where two sets of solutions were identified: a solution set A, characterised by large intrinsic diffusivity, intra-neurite fraction and dispersion (small κ), and a solution set B where low

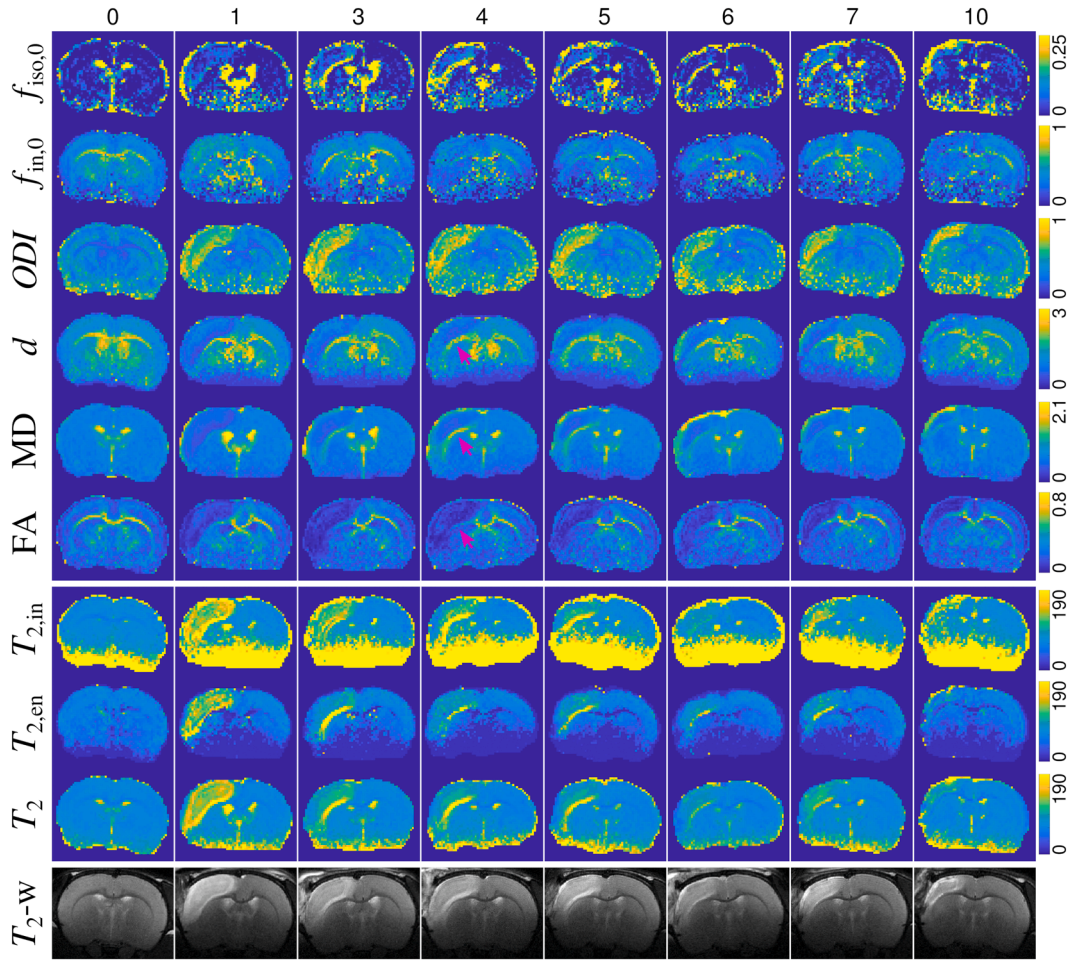

Fig. 7. Spatiotemporal evolution of MTE-NODDI parameter maps for a rat in group 2 (Bregma 0.48) along with MD, FA and T_2 maps from the DTIT$_2$ method. The top panel depicts the microstructure- and diffusion-related maps, the middle panel the relaxation-related maps and the bottom panel the high-resolution T2W images. The units for diffusion maps are μm^2/ms, while the units for relaxation times are ms.

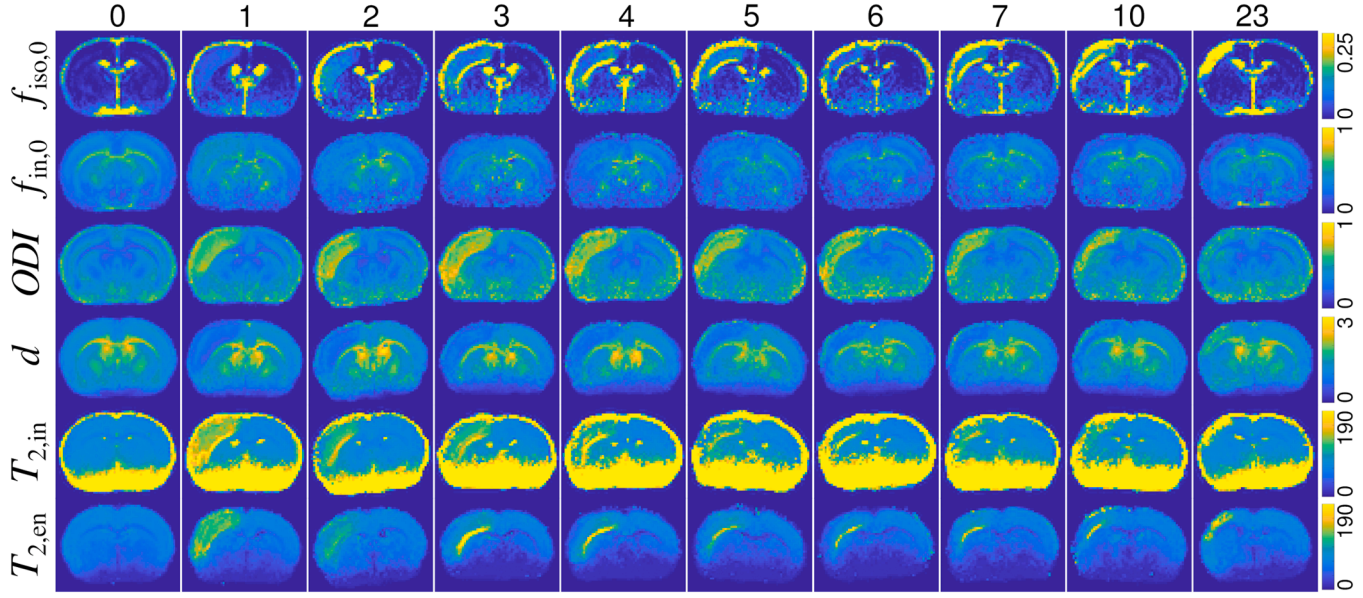

Fig. 8. Spatiotemporal evolution of MTE-NODDI parameter template maps obtained by averaging the maps from all animals within every time point (Bregma 0.48). The top panel depicts the microstructure- and diffusion-related maps, and the bottom panel the relaxation-related maps. The units for diffusion maps are μm^2/ms, while the units for relaxation times are ms.

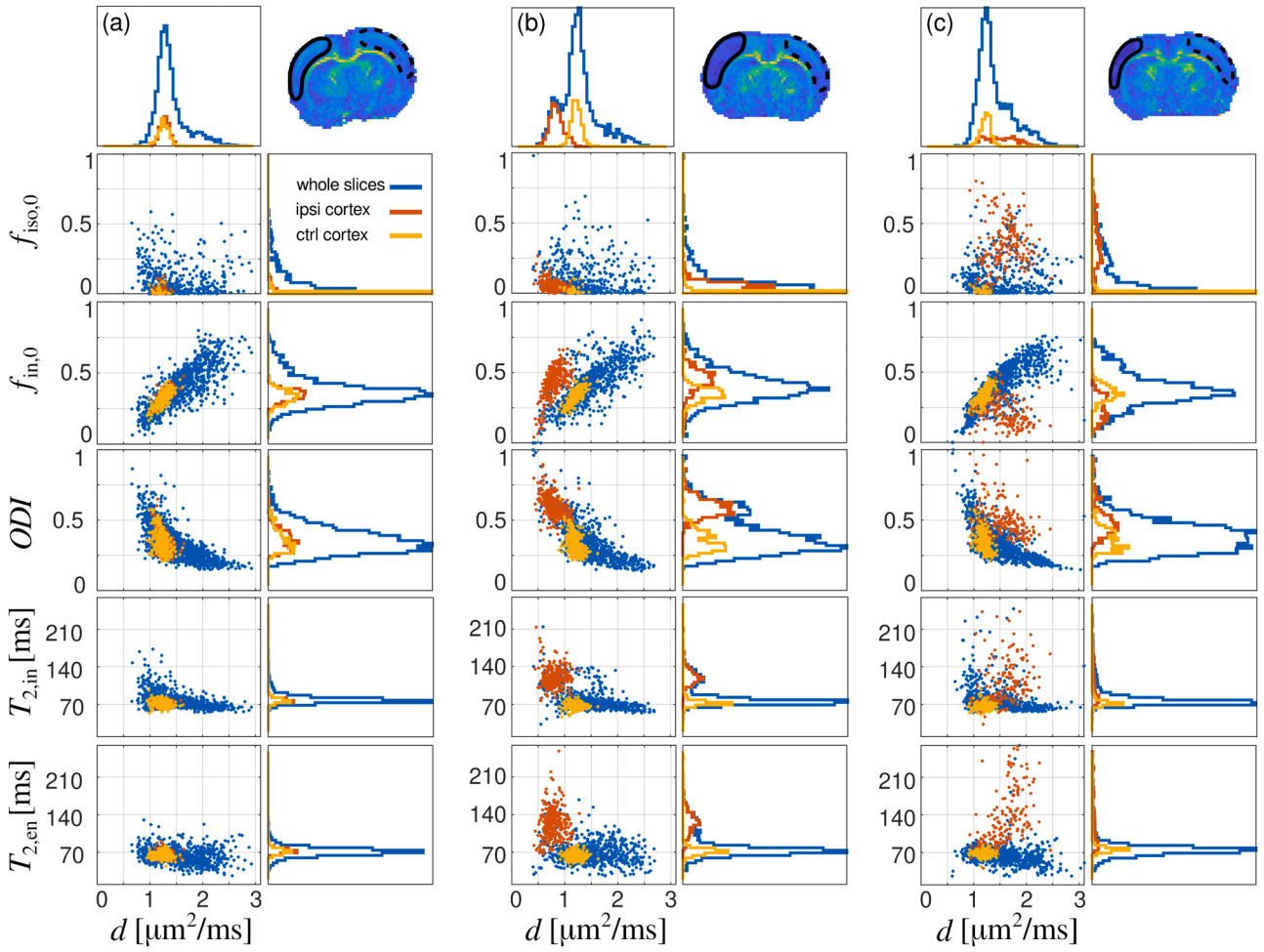

Fig. 9. Histograms of MTE-NODDI parameters taken over slices 1 and 2 (blue lines) and over ROIs drawn on the contralateral (yellow) and ipsilateral (red) cortices for a rat in group 1. Three representative time points were taken as examples: before stroke (a), and 1 (b) and 23 (c) days after stroke. The corresponding scatter plots of $f_{iso,0}$, $f_{in,0}$, *ODI*, $T_{2,in}$ and $T_{2,en}$ versus d are additionally shown. The ROIs are shown overlaid to the conventional FA from DTIT$_2$. Only voxels with SNR > 25 were considered. Voxels at the CSF-tissue interface located at the ventricles were additionally skipped.

Table 1
Spearman's rank correlation analysis of MTE-NODDI parameters versus d for two whole slices (ws), ROIs at the ipsilateral (ipsi) and contralateral (ctrl) cortices. *, $p < 0.05$; **, $p < 0.001$.

		$f_{iso,0}$ vs. d	$f_{in,0}$ vs. d	*ODI* vs. d	$T_{2,in}$ vs. d	$T_{2,en}$ vs. d
pre occlusion	ws	−0.07 *	0.84**	−0.65**	−0.38**	−0.19**
	ipsi	-	0.77**	−0.53**	-	-
	ctrl	-	0.77**	−0.52**	-	-
day 1	ws	−0.16**	0.44**	−0.79**	−0.49**	−0.39**
	ipsi	−0.39**	0.61**	−0.52**	0.19**	-
	ctrl	-	0.74**	−0.45**	-	-
day 23	ws	0.24**	0.61**	−0.54**	−0.10**	−0.14**
	ipsi	0.20 *	−0.47**	−0.14*	0.59**	0.72**
	ctrl	-	0.74**	−0.50**	-	-

intrinsic diffusivity, intra-neurite fraction and dispersion (large κ) were observed, which parallel the observations previously made in a similar model (Jelescu et al., 2016). Although both solutions are *a priori* biologically plausible, a number of works have favoured the prevalence of the solution associated with high dispersion (small κ) over that with low dispersion, for the in vivo brain tissue (Jelescu and Budde, 2017; Kunz et al., 2018; Szczepankiewicz et al., 2015; Veraart et al., 2017). Furthermore, the number of voxels in which solution B is achieved represents only ~8 % of the total slice, while this solution does not display spatial patterns coinciding with any anatomical region. The former arguments support the idea that solution A corresponds to the underlying substrate, thus justifying the suppression of solution B by adding an l_2-norm regularisation term to the least-squares cost function, which penalises the solutions characterised by large values of $\| \boldsymbol{\Omega} \|_2^2$, as a consequence of large κ values (see supplementary material S.2 for more details). In this regard, non-standard regularisation terms, e.g. $\lambda\kappa^2$, could show better performance than the standard approach utilised in this work and are, therefore, worth considering in future works.

Note that our approach resembles the method employed by Guerrero et al. (2019), in that both approaches rely on a minimisation of the square of the residuals, considering d as a variable. However, in contrast to the method employed by Guerrero et al. (2019), our approach performs the fitting simultaneously in all dimensions rather than using a two-step fitting process. Furthermore, our method does not require median filtering of the d maps, unlike Guerrero et al. (2019). Additionally, our approach for the estimation of κ and d also differs from that proposed by Howard et al. (2022), which relies on experimental data acquired at ultra-high b-values (where the signal from the extra neurite space can be neglected). Our approach can be applied to experimental data measured using medium-range b-values, i.e. $\lesssim$ 3.0 ms/μm^2, thus enabling wider applicability under conventional experimental settings. Moreover, the use of such medium-range b-values makes the estimated NODDI parameters less prone to differences in axonal diameter, as

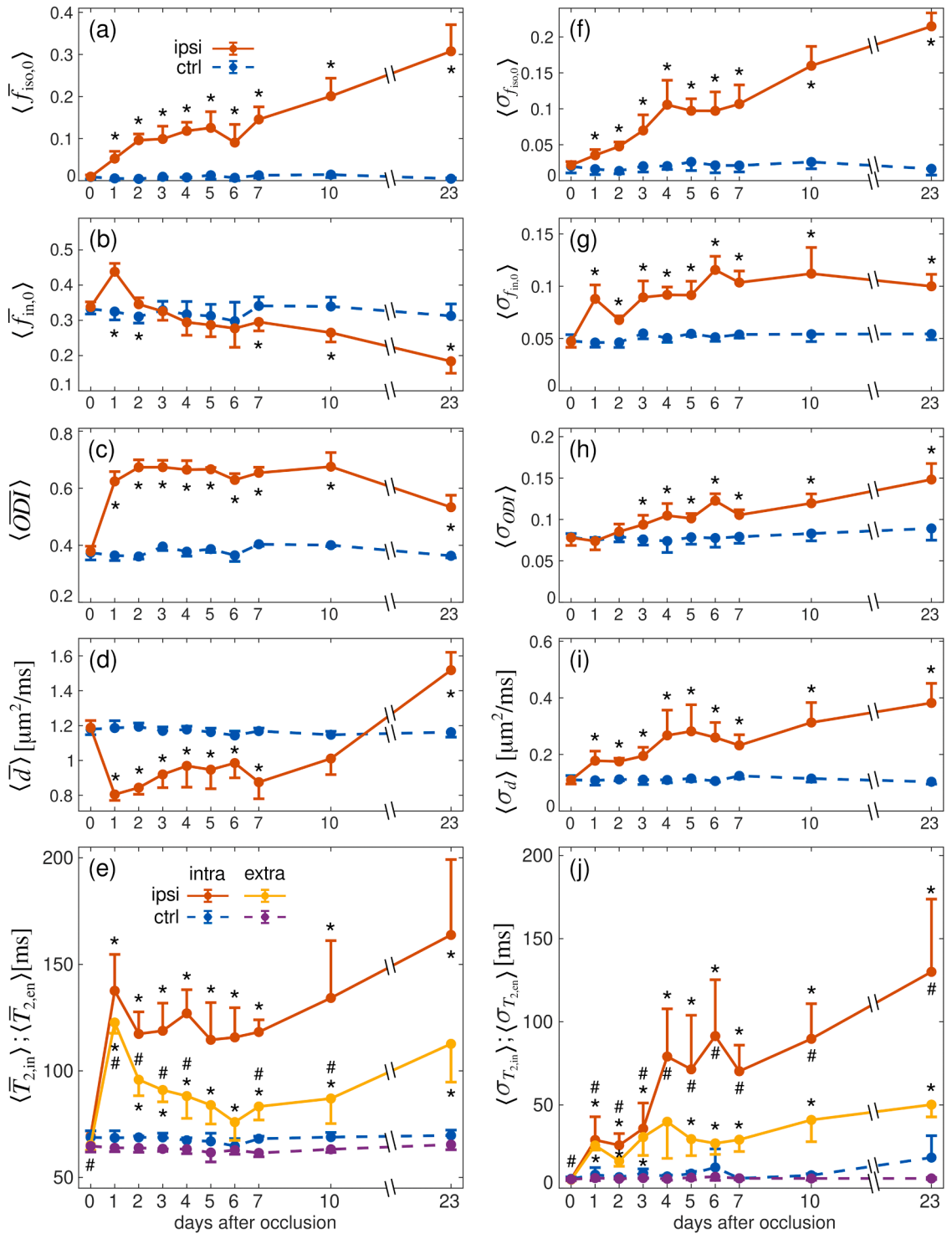

Fig. 10. (a-e) Temporal evolution of the mean, $\langle \overline{A} \rangle$, of MTE-NODDI parameters for ROIs drawn on the contralateral (blue dashed lines, also violet in (e)) and the ipsilateral (red solid lines, also yellow in (e)), taken over all animals in groups one and two and all time points. (f-j) Temporal evolution of the average standard deviation, $\langle \sigma_A \rangle$, for each parameter. Error bars denote the SEM. *, # $p < 0.05$.

discussed in other works (Howard et al., 2022; Veraart et al., 2020).

The spatial heterogeneity of d reported here further supports the consensus of a tissue-dependent NODDI intrinsic diffusivity (Guerrero et al., 2019; Howard et al., 2022). In our work, a mean value of 1.17 $\mu m^2/ms$ was measured for the healthy cortex, which is within the range of approximately [1.0,1.3] $\mu m^2/ms$ observed in some works (Fukutomi et al., 2018; Guerrero et al., 2019) based on adult, human GM. Conversely, a mean value of 2.04 $\mu m^2/ms$ was measured for WM tissue, which is above the range of approximately [1.6,1.8] $\mu m^2/ms$ measured by Guerrero et al. (2019), and within the range [2.0,2.5] $\mu m^2/ms$ reported by Howard et al. (2022) for adult humans. In this regard, the Spearman's rank correlation analysis showed different degrees of correlation between the newly assessed d and the remaining MTE-NODDI parameters. Nevertheless, these correlations do not disregard the complementary information provided by d, as shown by the rather large spread of points in the scatter plots (Fig. 9).

Regarding *ODI*, previous studies have investigated the correlation between the conventional *ODI* and histological measures (Grussu et al., 2017; Schilling et al., 2018; Wang et al., 2019). Notably, Schilling et al. (2018) showed that, among other MRI-based methods, *ODI* had the strongest correlation with its histological counterpart, although conventional *ODI* systematically overestimated the true dispersion. In the context of our results, one possible explanation for the overestimation could be the fact that releasing d effectively leads to lower *ODI* values compared to the case where d is fixed to values larger than the underlying substrate. However, corroboration of this hypothesis would require correlation with histological data.

The relaxation times, $T_{2,\mathrm{in}}$ and $T_{2,\mathrm{en}}$, measured in this study displayed similar histogram distributions between MTE-NODDI with fixed d versus that with released d (Fig. 3), except in voxels where $T_{2,\mathrm{en}}$ exhibited outliers. These findings align with the results published by Gong et al. (2020), who demonstrated only a slight negative bias in $T_{2,\mathrm{en}}$ when d was overestimated, a minor decrease in precision when d was underestimated, and no significant changes in $T_{2,\mathrm{in}}$ for varying d. This was also reflected in the low correlation seen in the scatter plots of $T_{2,\mathrm{in}}$ and $T_{2,\mathrm{en}}$ versus d in our results. The mean WM values in the ROIs for all animals prior to stroke are in agreement with the current consensus that $T_{2,\mathrm{in}} > T_{2,\mathrm{en}}$ for WM tissue (Benjamini and Basser, 2017; Gong et al., 2020; McKinnon and Jensen, 2019; Veraart et al., 2017). More specifically, the $T_{2,\mathrm{in}}$ values estimated in our work are slightly below the range [69,94] ms observed by Gong et al. (2020), and the range [64,94] ms reported by McKinnon and Jensen (2019). Conversely, $T_{2,\mathrm{en}}$ falls within the range [42,61] ms reported by Gong et al. (2020), but below the range [56,64] ms published by McKinnon and Jensen (2019). However, a direct comparison of absolute WM values is hampered by the proven dependence of these parameters on the relative orientation of the WM tract within the static magnetic field (McKinnon and Jensen, 2019). Regarding GM, the pre-stroke compartmental relaxation times averaged across all animals also suggest that the inequality $T_{2,\mathrm{in}} > T_{2,\mathrm{en}}$ holds true, although to a lesser extent. This trend is in agreement with the work by Benjamini and Basser (2017), who verified the condition $T_{2,\mathrm{in}} > T_{2,\mathrm{en}}$ for the intra-cellular and the interstitial GM. More generally, the whole-slice histogram distributions of $T_{2,\mathrm{in}}$ and $T_{2,\mathrm{en}}$ for healthy tissue presented here (Figs. 3 and 9) agree well with those shown in the original MTE-NODDI work (Gong et al., 2020), as well as with the TEdDI model by Veraart et al. (2017), despite the fact that the latter neglects the free diffusion compartment.

In terms of the assessment of the optimal regularisation parameter, several approaches have been previously utilised in the context of DW MRI, including empirical methods (Daducci et al., 2015; Landman et al., 2012) and *ad hoc* techniques such as the generalised cross-validation method (Golub et al., 1979). Here, we have chosen the more straightforward L-curve method, which has been previously used in DW MRI (Descoteaux et al., 2006). This method has the advantage of not requiring data simulation or prior knowledge. Consequently, it implicitly includes all nuisances associated with the experimental data. The synthetic data simulation demonstrated that the regularisation parameter computed using the L-curve method on in vivo data provides a fairly good minimisation of the bias, standard deviation and MSE of the simulated MTE-NODDI parameters. In this regard, it should be emphasised that, given the bimodal distribution exhibited by some of the MTE-NODDI parameters (see Fig. 4 and Fig. S.2), analysing only the bias may be misleading, as it can obscure meaningful differences between solution sets. In such scenarios, the MSE, which accounts for both bias and standard deviation, offers a more robust and interpretable metric for the overall performance of the estimator.

4.2. MTE-NODDI in ischaemic stroke

We have demonstrated that MTE-NODDI parameter maps offer unique, complementary contrast information that has the potential to probe the cascade of biophysical mechanisms occurring in ischemic tissue following stroke. In the following, we discuss the spatiotemporal evolution of such parameters in light of the current literature, while a biophysical interpretation is presented in the subsequent subsection.

A notable finding of this study is that the isotropic water fraction $f_{\mathrm{iso},0}$, as well as the TE-dependent counterparts, are significantly increased in the ischaemic cortex. This appears to contradict previous observations in human brain ischaemic stroke using NODDI, where a reduction of the isotropic fraction was reported (Adluru et al., 2014; Wang et al., 2019). This discrepancy may be attributed to the inverse relationship between $f_{\mathrm{iso},i}$ and d, as reported previously (Guerrero et al., 2019; Howard et al., 2022). Specifically, an overestimation of d leads to an underestimation of the isotropic fraction. Moreover, our results are consistent with previous works, where an increase in the free-diffusion water fraction, as evaluated using various free-water diffusion imaging techniques, was reported in both the acute and subacute phases of ischaemic stroke in rat (Farrher et al., 2021) and human (Nägele et al., 2024) brain tissues. Crucially, the fact that the isotropic fraction at the ipsilateral cortex is significantly elevated suggests that other models, such as TEdDI (Veraart et al., 2017) (in DW-T2W experiments), NODDIDa (Jelescu et al., 2016) and others (Kaden et al., 2016) (in DW experiments), may be inappropriate for the investigation of ischemic tissue due to absence of this fraction in the model.

Another key technical outcome of the present work is that the collapse of $f_{\mathrm{in},i}$ to unity in the early phases of stroke (Fig. 3) for fixed, overestimated d (which further translates as an outlier in both $f_{\mathrm{in},0}$ and $T_{2,\mathrm{en}}$) is mitigated by releasing d. Our group has previously reported this feature in a preliminary work (Farrher et al., 2023) where the collapse of $f_{\mathrm{in},i}$ (and $f_{\mathrm{in},0}$) was avoided by using fixed values of $d < 1.7$ $\mu m^2/ms$. Moreover, this feature in $f_{\mathrm{in},i}$ within the framework of NODDI in ischaemic tissue has also previously been observed in both animals (Wang et al., 2021) and humans (Wang et al., 2019), although explicit discussion of its implications was not provided by the authors. We have demonstrated that $f_{\mathrm{in},0}$ appears elevated in the ischaemic tissue one day after stroke, even when d is released. More generally, the evolution of $f_{\mathrm{in},0}$ during the different phases of stroke is tendentially (yet not in absolute values) comparable to that of the intra-neurite fraction estimated using conventional NODDI and other biophysical models (Bagdasarian et al., 2021; Hui et al., 2012b; Kellner et al., 2022). Kellner et al. (2022) observed an increase of ~50 % (roughly estimated based on their charts) in human WM during the hyperacute phase (a median of 132 min after stroke), using the diffusion microstructure imaging approach (Reisert et al., 2017). At a mean of ~42 h after stroke, Hui et al. (2012b) reported a milder increase of ~10 % in human WM, which was evaluated with the help of the white matter tract integrity model (Fieremans et al., 2011), and in agreement with the trend towards renormalisation with time seen in our work. Furthermore, in a study using conventional NODDI in WM at the late subacute (14 days) and chronic (231 days) phases, Mastropietro et al. (2019) reported no significant changes (late subacute phase) and a significant reduction (chronic phase) of the intra-neurite fraction, also in agreement with our results. However, the former appears to conflict with the results reported by Wang et al. (2019), where an average increase in the intra-neurite fraction of ~61 % was shown for subjects measured between 3 days and 2 weeks after stroke. These discrepancies emphasise the need for further studies in order to clearly elucidate the spatiotemporal evolution of this parameter.

Conventional *ODI* has been shown to have high sensitivity to tissue microstructural changes during ischaemic stroke (Adluru et al., 2014; Bagdasarian et al., 2021; Mastropietro et al., 2019; Wang et al., 2019; Wang et al., 2021). We demonstrated that the increase in *ODI* is milder for the case with free d compared to that with fixed, overestimated d (Fig. 3). More generally, the increment in *ODI* during the acute and subacute phases seen in this work is also consistent with the trends previously observed in human WM (Mastropietro et al., 2019; Wang et al., 2019) and rat GM (Bagdasarian et al., 2021; Wang et al., 2021).

However, Bagdasarian et al. (2021) reported only a small, not significant rise in *ODI* in the rat external capsule. Finally, during the chronic phase only a slight increase in *ODI*, smaller in magnitude than in previous phases, in the ischemic striatum (Bagdasarian et al., 2021) and WM (Bagdasarian et al., 2021; Mastropietro et al., 2019) was reported, which is also in agreement with our results.

The decline in d during the acute and subacute phases witnessed here is in agreement with that observed in the compartmental diffusivities provided by similar models. For instance, Kellner et al. (2022) reported a reduction in all diffusivities (axial intra-neurite as well as axial and radial extra-neurite) in human WM during the hyperacute phase. Similarly, Hui et al. (2012b) reported a reduction in the same three compartmental diffusivities in the human brain at a mean of ~42 h after stroke onset. Interestingly, the highest degree of change was observed in the intra-axonal diffusivity in both publications. However, it is important to emphasise that the models mentioned above are intrinsically different from NODDI, particularly in that the axial intra- and extra-neurite diffusivities in NODDI are constrained to be equal, and the radial extra-neurite diffusivity directly depends on d via the tortuosity model (Szafer et al., 1995; Zhang et al., 2012).

Qualitatively, the spatiotemporal evolution of $T_{2,\mathrm{in}}$ and $T_{2,\mathrm{en}}$ is comparable to that of conventional T_2, which has been thoroughly investigated in the literature on MCAo models (Carano et al., 2000; Farrher et al., 2021; Lin et al., 2002; Lin et al., 2002; Sotak, 2002; Wagner et al., 2012). Coarsely, it can be divided into three phases. Firstly, an initial, rather homogeneous increase during the acute phase, which peaks between 24 and 48 h after stroke onset, has been described. Afterwards, during the subacute phase, the ischaemic cortex displays a heterogeneous evolution where the ischemic core experiences a transient renormalisation, while the surrounding border zone tends to show steadily higher values. Finally, during the late subacute and chronic phases, the ischaemic core displays a further increase, which finally leads to a homogeneously increased T_2 in the whole ischaemic cortex. Crucially, however, we have demonstrated that $T_{2,\mathrm{in}}$ and $T_{2,\mathrm{en}}$ not only exhibit significant differences during the various phases of stroke, but also display different patterns of spatial heterogeneity (Fig. 10). This underscores the potentially complementary insights these parameters provide into tissue condition.

4.3. A digression on the biophysical picture

The biophysical mechanisms occurring during the first 24 to 48 h after MCAo include cellular swelling (Knight et al., 1991) and neurite beading (Budde and Frank, 2010) as a result of cytotoxic oedema, which is consistent with the increase in $f_{\mathrm{in},0}$ and the decrease in d reported here. A well-known feature that occurs as a consequence of these mechanisms, is a reduction in conventional MD (Carano et al., 2000; Grinberg et al., 2014, 2012; Hui et al., 2012a, 2012b). In this regard, Hui et al. (2012b) demonstrated that the dominant factor leading to the decrease in MD during the subacute phase is a reduction in the axial intra-axonal diffusivity (46 %), whereas a smaller increase (10 %) in the axonal water fraction was measured in human WM. This tendency aligns with our results in ischaemic GM, where although the magnitude of change in $f_{\mathrm{in},0}$ one day after stroke (35 %) is similar to that of d (32 %), from day two onwards, $f_{\mathrm{in},0}$ displays a trend towards renormalisation, whereas d remains at significantly lower-than-normal values. However, it should be noted that NODDI fundamentally blends the contribution of soma, microglia, astrocytes, interstitial space and other types of cells into a single compartment, namely the extra-neurite space. Therefore, the increase in $f_{\mathrm{in},0}$ in acute stroke only refers to the increase in the intra-neurite space, whereas the characteristic soma swelling of cytotoxic oedema is not captured by the current model. Likewise, the obviation of the soma compartment, may represent a potentially confounding factor in the interpretation of other variables associated with the tissue compartment.

Another mechanism that occurs during the acute and early subacute phases of stroke is an increase in tissue water content (Carano et al., 2000; Helpern et al., 1993; Knight et al., 1991; Lin et al., 2002; Pierpaoli et al., 1993; Wagner et al., 2012) and the development of tissue vacuolation (Farrher et al., 2021; Helpern et al., 1993; Nägele et al., 2024). These changes are thought to be responsible for the increase in the conventional T_2 (Knight et al., 1991; Lin et al., 2002; Matsumoto et al., 1995; Wagner et al., 2012) and the free-diffusion fraction (Farrher et al., 2021; Nägele et al., 2024), which is also consistent with the increment in $T_{2,\mathrm{in}}$, $T_{2,\mathrm{en}}$ and $f_{\mathrm{iso},0}$ reported here. Remarkably, the inequality $T_{2,\mathrm{in}} > T_{2,\mathrm{en}}$ holds true for the whole investigated time window. Although not yet well understood, this inequality has been explained for WM in terms of different exchange rates between the myelin and the intra/extra-axonal water pools due to differences in the surface-to-volume ratio of the two compartments and the effect of the axonal membrane that, collectively, retard the exchange between the myelin and the intra-axonal water pools (Gong et al., 2020; Lin et al., 2018; Nilsson et al., 2010; Veraart et al., 2017). In the case of GM, the smaller difference between both relaxation times is likely a consequence of the relatively lower fraction of myelinated axons. Hence, the differing spatiotemporal progression of $T_{2,\mathrm{in}}$ and $T_{2,\mathrm{en}}$ likely holds the potential to discern the relevance that the former mechanisms have throughout the development of ischaemia. Nevertheless, more dedicated experimental data and histopathological analyses are needed in order to further elucidate these hypotheses.

During the subacute phase, the conventional MD and T_2 are known to have a heterogeneous evolution, where the core (or necrotic) zone displays a trend towards renormalisation and the border (or clearance) zone shows steadily elevated values (Farrher et al., 2021; Hui et al., 2012a; Lin et al., 2002; Lin et al., 2002; Wagner et al., 2012). The proposed mechanisms to explain the former include drainage and an increase in the binding of free water by degraded proteins, whereas the latter has been interpreted in terms of tissue liquefaction and perivascular oedema (Farrher et al., 2021; Lin et al., 2002; Lin et al., 2002; Wagner et al., 2012). Conversely, the conventional FA displays a rather homogeneous temporal progression (Farrher et al., 2021). Interestingly, some MTE-NODDI parameters, namely $f_{\mathrm{iso},0}$, d, $T_{2,\mathrm{in}}$ and $T_{2,\mathrm{en}}$ seem to parallel the heterogeneous spatiotemporal patterns of conventional MD and T_2, whereas $f_{\mathrm{in},0}$ and *ODI* display rather homogeneous patterns, similar to the case of conventional FA.

Evidence in the literature suggests that a change in *ODI* may have different substrates, depending on the tissue under consideration. For example, in an in vitro study on multiple sclerosis, Grussu et al. (2017) linked a reduction in *ODI* with focal demyelination and the consequent reduced geometrical complexity in the axon architecture of the human spinal cord. Conversely, a reduction in *ODI* at the cortex may indicate a reduction in the complexity of dendritic arborisations (Grussu et al., 2017). Interestingly, the temporal evolution of *ODI* appears negatively correlated with that of the conventional FA (Farrher et al., 2021; Hui et al., 2012a; Mastropietro et al., 2019). This result, together with the minor change seen in $f_{\mathrm{in},0}$ during the same time window, suggests that the dominant mechanism inducing the typically observed reduction in FA may likely be an increase in the neurite orientation dispersion, whereas a reduction in the neurite density may be less important.

4.4. Clinical relevance

An important aspect that hinders the application of MTE-NODDI in clinical practice is its long acquisition time. In this regard, our estimation approach based on the simultaneous analysis of all T2W experiments enables more flexible experimental setups compared to the original MTE-NODDI, where the same DW experiment must be performed for each TE. Additionally, optimisation approaches, such as the minimisation of the Cramér-Rao lower bound of the parameters, in combination with appropriate parametrisation of the experimental

settings, could be utilised to further reduce the acquisition time (Collier et al., 2017; Gras et al., 2017; Poot et al., 2010).

Although a large proportion of research into diffusion and relaxometry MRI in stroke focuses on the hyperacute phase and the early detection after onset, some works have demonstrated that conventional *ODI* offers unique information on motor outcomes after stroke (DiBella et al., 2022; Hodgson et al., 2019; Mastropietro et al., 2019). In this regard, it is expected that MTE-NODDI parameters may not only improve the comparability and reproducibility between studies and/or institutions via the use of the TE-independent compartmental fractions but may also provide unique physiological insight into tissue condition and outcome.

An important topic within the stroke community relates to the segmentation of affected tissue. In this regard, Kellner et al. (2022) demonstrated that the axial intra-neurite diffusivity provides a superior contrast between ischaemic and healthy tissue compared to that of conventional DW MRI models. This, in turn, leads to higher accuracy and precision in the delineation of the infarcted tissue. Similarly, we hypothesise that the newly estimated d could also provide complementary information for tissue segmentation approaches. More generally, it is expected that multiparametric-based machine learning segmentation approaches (Benzakoun et al., 2021; Lee et al., 2020) may also benefit from the heterogeneous spatiotemporal progression of MTE-NODDI parameters after stroke.

5. Limitations

While the MTE-NODDI parameters exhibited trends consistent with the expected sensitivity to the hypothesised biophysical property, it is important to interpret these parameters strictly within the framework of NODDI (or MTE-NODDI). Indeed, besides the limitation regarding the fixation of d, the soundness of the axial, intra- and extra-neurite diffusivity being equal has been addressed in several papers, where the idea of the former being larger than the latter seems to prevail (Kunz et al., 2018; Reisert et al., 2017; Szczepankiewicz et al., 2015; Veraart et al., 2017). Similarly, the validity of the tortuosity model has been questioned, particularly in cases of tightly packed axons (Jelescu and Budde, 2017; Novikov and Fieremans, 2012). Moreover, the assumption of a negligible exchange between compartments, which may be significant during the acute phase of ischaemic stroke, has also been challenged by several authors (Jelescu et al., 2022; Lampinen et al., 2021; Lätt et al., 2009; Zhang et al., 2021). For a more detailed discussion on the former topics, the reader is referred to the following reviews (Jelescu and Budde, 2017; Kamiya et al., 2020; Lampinen et al., 2023).

In the particular case of GM, although NODDI was originally introduced as a tool to assess tissue microstructural complexity in both GM and WM (Zhang et al., 2012), the validity of the model assumptions in GM has been challenged in several works. In particular, NODDI does not explicitly account for the soma compartment in GM. Hence, more sophisticated models able to capture soma characteristics, such as SANDI (Palombo et al., 2020), would be advantageous in studies of ischaemic stroke. Nevertheless, the neglect of the soma compartment has been shown to become significant for b-values > 3 ms/μm^2 (Palombo et al., 2020), which is beyond the b-value range utilised in our work.

Another limitation of the current study is the sample size, which reduces statistical power and poses a limitation to the generalisability of our results. Moreover, the lack of direct histological validation represents a limitation to the interpretation of the results. This emphasises the need for further studies, where direct histological data are acquired in parallel to MRI data.

One aspect that hinders the direct application of the present estimation approach is the lengthy data postprocessing time, which on an Intel Core i9, 8th Gen processor with six parallel workers needs approximately 1.5 h per slice. In this regard, convex optimisation approaches such as AMICO (Daducci et al., 2015) could potentially help reduce the postprocessing time. In this context, more advanced estimation approaches, such as the deep learning-based Bayesian method proposed by Jallais and Palombo (2024), could be beneficial for these kinds of models, displaying highly degenerate landscapes.

Finally, a detailed analysis of the ischaemic WM was hampered by the reduced image resolution, which hindered an accurate segmentation of the external capsule. However, as known from the literature, the signature of ischaemic stroke in the DW signal (especially at high b-values) in WM is different from that of GM (Hui et al., 2012b; Jensen et al., 2011), emphasising the need for further studies employing higher spatial resolution.

6. Conclusions

This study has demonstrated that the assessment of ischaemic tissue after MCAo using MTE-NODDI with released intrinsic diffusivity is feasible by incorporating an l_2-norm regularisation term in the least-squares cost function. The findings also indicate that some of the shortcomings of conventional MTE-NODDI in ischaemic tissue (e.g. the underestimation of the free-diffusion fraction and the overestimation of the intra-neurite fraction) can be mitigated by releasing the intrinsic diffusivity. Moreover, the evolution of the newly estimated MTE-NODDI parameters was shown to be heterogeneous and heterochronous, with parameters such as the intra-neurite fraction and the orientation dispersion index showing rather homogenous values within the ischaemic cortex throughout the time course of the study. On the other hand, parameters such as the free-diffusion fraction and the intra-/extra-neurite T2 times displayed heterogeneous spatial distributions, highlighting differences between the ischaemic core and border zone. Hence, this new set of relaxation- and diffusion-related parameters have the potential to both deepen our understanding of the biophysical mechanisms triggered after stroke onset, as well as the monitoring of tissue evolution and prediction of stroke outcome.

Data availability

Experimental data published in this work and scripts will be available via formal request to the corresponding authors and a signed data-sharing agreement.

CRediT authorship contribution statement

Ezequiel Farrher: Writing – review & editing, Writing – original draft, Visualization, Supervision, Software, Project administration, Methodology, Investigation, Formal analysis, Conceptualization. **Kuan-Hung Cho:** Writing – review & editing, Supervision, Software, Project administration, Methodology, Investigation, Formal analysis, Data curation, Conceptualization. **Chia-Wen Chiang:** Writing – review & editing, Supervision, Software, Project administration, Methodology, Investigation, Formal analysis, Data curation, Conceptualization. **Ming-Jye Chen:** Writing – review & editing, Supervision, Project administration, Methodology, Investigation, Data curation, Conceptualization. **Sheng-Min Huang:** Writing – review & editing, Methodology, Investigation, Data curation. **Li-Wei Kuo:** Writing – review & editing, Supervision, Resources, Project administration, Methodology, Investigation, Funding acquisition, Conceptualization. **Chang-Hoon Choi:** Writing – review & editing, Supervision, Resources, Project administration, Methodology, Investigation, Funding acquisition, Conceptualization. **N. Jon Shah:** Writing – review & editing, Resources, Project administration, Funding acquisition.

Declaration of competing interest

The authors declare that they have no known competing financial interests or personal relationships that could have appeared to influence the work reported in this paper.

Acknowledgements

EF thanks Dr. P. Pais Roldan for valuable discussions. We thank Dr. J. Felder and Dr. M. Zimmermann for their technical support in using the computer cluster, Dr. Yun Wang and Dr. Kuo-Jen Wu for their support in making the MACo rat model, and Ms. C. Rick for proofreading the manuscript. CHC would like to acknowledge DAAD (57654162) for their support in this research collaboration. LWK would like to thank NHRI (NHRI-BN-113-PP-06) and NSTC (113-2927-I-400-501) for their support in this joint research.

Supplementary materials

Supplementary material associated with this article can be found, in the online version, at doi:10.1016/j.neuroimage.2025.121390.

References

Adluru, G., Gur, Y., Anderson, J.S., Richards, L.G., Adluru, N., Dibella, E.V.R., 2014. Assessment of white matter microstructure in stroke patients using NODDI. In: 2014 36th Annual International Conference of the IEEE Engineering in Medicine and Biology Society, 2014. EMBC, pp. 742–745. https://doi.org/10.1109/EMBC.2014.6943697.

Andersson, J.L.R., Skare, S., Ashburner, J., 2003. How to correct susceptibility distortions in spin-echo echo-planar images: application to diffusion tensor imaging. Neuroimage 20, 870–888. https://doi.org/10.1016/S1053-8119(03)00336-7.

Avants, B.B., Tustison, N.J., Song, G., Cook, P.A., Klein, A., Gee, J.C., 2011. A reproducible evaluation of ANTs similarity metric performance in brain image registration. Neuroimage 54, 2033–2044. https://doi.org/10.1016/j.neuroimage.2010.09.025.

Bagdasarian, F.A., Yuan, X., Athey, J., Bunnell, B.A., Grant, S.C., 2021. NODDI highlights recovery mechanisms in white and gray matter in ischemic stroke following human stem cell treatment. Magn. Reson. Med. 86. https://doi.org/10.1002/mrm.28929.

Benjamini, D., Basser, P.J., 2017. Magnetic resonance microdynamic imaging reveals distinct tissue microenvironments. Neuroimage 163. https://doi.org/10.1016/j.neuroimage.2017.09.033.

Benzakoun, J., Charron, S., Turc, G., Hassen, W.Ben, Legrand, L., Boulouis, G., Naggara, O., Baron, J.C., Thirion, B., Oppenheim, C., 2021. Tissue outcome prediction in hyperacute ischemic stroke: comparison of machine learning models. J. Cereb. Blood Flow Metab. 41, 3085–3096. https://doi.org/10.1177/0271678X211024371.

Bouyagoub, S., Dowell, N.G., Hurley, S.A., Mara Cercignani, T.C., 2016. Overestimation of CSF fraction in NODDI: possible correction techniques and the effect on neurite density and orientation dispersion measures. In: Proceedings of the International Society for Magnetic Resonance in Medicine, p. 0007.

Budde, M.D., Frank, J.A., 2010. Neurite beading is sufficient to decrease the apparent diffusion coefficient after ischemic stroke. Proc. Natl. Acad. Sci. U.S.A. 107, 14472–14477. https://doi.org/10.1073/pnas.1004841107.

Carano, R.A.D., Li, F., Irie, K., Helmer, K.G., Silva, M.D., Fisher, M., Sotak, C.H., 2000. Multispectral analysis of the temporal evolution of cerebral ischemia in the rat brain. J. Magn. Reson. Imaging 12, 842–858. https://doi.org/10.1002/1522-2586(200012)12:6<842::AID-JMRI7>3.0.CO;2-5.

Caverzasi, E., Papinutto, N., Castellano, A., Zhu, A.H., Scifo, P., Riva, M., Bello, L., Falini, A., Bharatha, A., Henry, R.G., 2016. Neurite orientation dispersion and density imaging color maps to characterize brain diffusion in neurologic disorders. J. Neuroimaging 26. https://doi.org/10.1111/jon.12359.

Chen, S.T., Hsu, C.Y., Hogan, E.L., Maricq, H., Balentine, J.D., 1986. A model of focal ischemic stroke in the rat: reproducible extensive cortical infarction. Stroke 17, 738–743. https://doi.org/10.1161/01.STR.17.4.738.

Cho, K.-H., Huang, S.-M., Choi, C.-H., Chen, M.-J., Chiang, H.-H., Buschbeck, R.P., Farrher, E., Shah, N.J., Garipov, R., Chang, C.-P., Chang, H., Kuo, L.-W., 2019. Development, integration and use of an ultrahigh-strength gradient system on a human-size 3 T magnet for small animal MRI. PLoS One 14, e0217916. https://doi.org/10.1371/journal.pone.0217916.

Colgan, N., Siow, B., O'Callaghan, J.M., Harrison, I.F., Wells, J.A., Holmes, H.E., Ismail, O., Richardson, S., Alexander, D.C., Collins, E.C., Fisher, E.M., Johnson, R., Schwarz, A.J., Ahmed, Z., O'Neill, M.J., Murray, T.K., Zhang, H., Lythgoe, M.F., 2016. Application of neurite orientation dispersion and density imaging (NODDI) to a tau pathology model of Alzheimer's disease. Neuroimage 125, 739–744. https://doi.org/10.1016/j.neuroimage.2015.10.043.

Collier, Q., Veraart, J., den Dekker, A.J., Vanhevel, F., Parizel, P.M., Sijbers, J., 2017. Solving the free water elimination estimation problem by incorporating T2 relaxation properties. In: Proceedings of the International Society for Magnetic Resonance in Medicine, p. 1783.

Collier, Q., Veraart, J., Jeurissen, B., Vanhevel, F., Pullens, P., Parizel, P.M., den Dekker, A.J., Sijbers, J., 2018. Diffusion kurtosis imaging with free water elimination: a bayesian estimation approach. Magn. Reson. Med. 80, 802–813. https://doi.org/10.1002/mrm.27075.

Crombe, A., Planche, V., Raffard, G., Bourel, J., Dubourdieu, N., Panatier, A., Fukutomi, H., Dousset, V., Oliet, S., Hiba, B., Tourdias, T., 2018. Deciphering the microstructure of hippocampal subfields with in vivo DTI and NODDI: applications to experimental multiple sclerosis. Neuroimage 172, 357–368. https://doi.org/10.1016/j.neuroimage.2018.01.061.

Daducci, A., Canales-Rodríguez, E.J., Zhang, H., Dyrby, T.B., Alexander, D.C., Thiran, J. P., 2015. Accelerated microstructure imaging via Convex optimization (AMICO) from diffusion MRI data. Neuroimage 105, 32–44. https://doi.org/10.1016/j.neuroimage.2014.10.026.

Descoteaux, M., Angelino, E., Fitzgibbons, S., Deriche, R., 2006. Apparent diffusion coefficients from high angular resolution diffusion imaging: estimation and applications. Magn. Reson. Med. 56, 395–410. https://doi.org/10.1002/mrm.20948.

DiBella, E.V.R., Sharma, A., Richards, L., Prabhakaran, V., Majersik, J.J., HashemizadehKolowri, S.K., 2022. Beyond diffusion tensor MRI methods for improved characterization of the brain after ischemic stroke: a review. Am. J. Neuroradiol. https://doi.org/10.3174/ajnr.A7414.

Dortch, R.D., Apker, G.A., Valentine, W.M., Lai, B., Does, M.D., 2010. Compartment-specific enhancement of white matter and nerve ex vivo using chromium. Magn. Reson. Med. 64, 688–697. https://doi.org/10.1002/mrm.22460.

Fan, R.H., Does, M.D., 2008. Compartmental relaxation and diffusion tensor imaging measurements in vivo in λ-carrageenan-induced edema in rat skeletal muscle. NMR Biomed. 21, 566–573. https://doi.org/10.1002/nbm.1226.

Farrher, E., Chiang, C.-W., Cho, K.-H., Grinberg, F., Buschbeck, R.P., Chen, M.-J., Wu, K.-J., Wang, Y., Huang, S.-M., Abbas, Z., Choi, C.-H., Shah, N.J., Kuo, L.W., 2021. Spatiotemporal characterisation of ischaemic lesions in transient stroke animal models using diffusion free water elimination and mapping MRI with echo time dependence. Neuroimage 244, 118605. https://doi.org/10.1016/J.NEUROIMAGE.2021.118605.

Farrher, E., Chiang, C.-W., Choi, C.-H., Cho, K.-H., Huang, S.-M., Chen, M.-J., Kuo, L.-W., Shah, N.J., 2023. Multi-echo NODDI for the study of tissue compartmentalisation in transient ischaemic stroke: initial insights. In: Proceedings of the International Society for Magnetic Resonance in Medicine, p. 4303.

Farrher, E., Grinberg, F., Kuo, L.-W., Cho, K.H., Buschbeck, R.P., Chen, M.-J., Chiang, H.-H., Choi, C.-H., Shah, N.J., 2020. Dedicated diffusion phantoms for the investigation of free water elimination and mapping: insights into the influence of T2 relaxation properties. NMR Biomed. 33, e4210. https://doi.org/10.1002/nbm.4210.

Fieremans, E., Jensen, J.H., Helpern, J.A., 2011. White matter characterization with diffusional kurtosis imaging. Neuroimage 58, 177–188. https://doi.org/10.1016/j.neuroimage.2011.06.006.

Fukutomi, H., Glasser, M.F., Zhang, H., Autio, J.A., Coalson, T.S., Okada, T., Togashi, K., Van Essen, D.C., Hayashi, T., 2018. Neurite imaging reveals microstructural variations in human cerebral cortical gray matter. Neuroimage 182, 488–499. https://doi.org/10.1016/j.neuroimage.2018.02.017.

Garcia, D., 2010. Robust smoothing of gridded data in one and higher dimensions with missing values. Comput. Stat. Data Anal. 54, 1167–1178. https://doi.org/10.1016/j.csda.2009.09.020.

Gazdzinski, L.M., Mellerup, M., Wang, T., Adel, S.A.A., Lerch, J.P., Sled, J.G., Nieman, B. J., Wheeler, A.L., 2020. White matter changes caused by mild traumatic brain injury in mice evaluated using neurite orientation dispersion and density imaging. J. Neurotrauma 37, 1818–1828. https://doi.org/10.1089/neu.2020.6992.

Golub, G.H., Heath, M., Wahba, G., 1979. Generalized cross-validation as a method for choosing a good ridge parameter. Technometrics 21, 215–223. https://doi.org/10.1080/00401706.1979.10489751.

Gong, T., Tong, Q., He, H., Sun, Y., Zhong, J., Zhang, H., 2020. MTE-NODDI: multi-TE NODDI for disentangling non-T2-weighted signal fractions from compartment-specific T2 relaxation times. Neuroimage 217, 116906. https://doi.org/10.1016/j.neuroimage.2020.116906.

Gras, V., Farrher, E., Grinberg, F., Shah, N.J., 2017. Diffusion-weighted DESS protocol optimization for simultaneous mapping of the mean diffusivity, proton density and relaxation times at 3 tesla. Magn. Reson. Med. 78. https://doi.org/10.1002/mrm.26353.

Grinberg, F., Ciobanu, L., Farrher, E., Shah, N.J., 2012. Diffusion kurtosis imaging and log-normal distribution function imaging enhance the visualisation of lesions in animal stroke models. NMR Biomed. 25. https://doi.org/10.1002/nbm.2802.

Grinberg, F., Farrher, E., Ciobanu, L., Geffroy, F., Le Bihan, D., Shah, N.J., 2014. Non-Gaussian diffusion imaging for enhanced contrast of brain tissue affected by ischemic stroke. PLoS One 9, e89225. https://doi.org/10.1371/journal.pone.0089225.

Grussu, F., Schneider, T., Tur, C., Yates, R.L., Tachrount, M., Ianuş, A., Yiannakas, M.C., Newcombe, J., Zhang, H., Alexander, D.C., DeLuca, G.C., Gandini Wheeler-Kingshott, C.A.M., 2017. Neurite dispersion: a new marker of multiple sclerosis spinal cord pathology? Ann. Clin. Transl. Neurol. 4, 663–679. https://doi.org/10.1002/acn3.445.

Gudbjartsson, H., Patz, S., 1995. The rician distribution of noisy MRI data. Magn. Reson. Med. 34, 910–914.

Guerrero, J.M., Adluru, N., Bendlin, B.B., Goldsmith, H.H., Schaefer, S.M., Davidson, R. J., Kecskemeti, S.R., Zhang, H., Alexander, A.L., 2019. Optimizing the intrinsic parallel diffusivity in NODDI: an extensive empirical evaluation. PLoS One 14, e0217118. https://doi.org/10.1371/journal.pone.0217118.

Hansen, P.C., 2000. The L-curve and its use in the numerical treatment of inverse problems. Comput. Inverse Probl. Electrocardiology 4, 119–142 ed. P. Johnston, Adv. Comput. Bioeng.

Helpern, J.A., Dereski, M.O., Knight, R.A., Ordidge, R.J., Chopp, M., Qing, Z.X., 1993. Histopathological correlations of nuclear magnetic resonance imaging parameters in experimental cerebral ischemia. Magn. Reson. Imaging 11, 241–246. https://doi.org/10.1016/0730-725X(93)90028-C.

Hodgson, K., Adluru, G., Richards, L.G., Majersik, J.J., Stoddard, G., Adluru, N., Di Bella, E., 2019. Predicting motor outcomes in stroke patients using diffusion

spectrum MRI microstructural measures. Front. Neurol. 10, 72. https://doi.org/10.3389/fneur.2019.00072.
Howard, A.F., Cottaar, M., Drakesmith, M., Fan, Q., Huang, S.Y., Jones, D.K., Lange, F.J., Mollink, J., Rudrapatna, S.U., Tian, Q., Miller, K.L., Jbabdi, S., 2022. Estimating axial diffusivity in the NODDI model. Neuroimage 262, 119535. https://doi.org/10.1016/j.neuroimage.2022.119535.
Hui, E.S., Du, F., Huang, S., Shen, Q., Duong, T.Q., 2012a. Spatiotemporal dynamics of diffusional kurtosis, mean diffusivity and perfusion changes in experimental stroke. Brain Res 1451, 100–109. https://doi.org/10.1016/j.brainres.2012.02.044.
Hui, E.S., Fieremans, E., Jensen, J.H., Tabesh, A., Feng, W., Bonilha, L., Spampinato, M. V., Adams, R., Helpern, J.A., 2012b. Stroke assessment with diffusional kurtosis imaging. Stroke 43, 2968–2973. https://doi.org/10.1161/STROKEAHA.112.657742.
Jallais, M., Palombo, M., 2024. Introducing μGUIDE for quantitative imaging via generalized uncertainty-driven inference using deep learning. Elife 13, RP101069. https://doi.org/10.7554/eLife.101069.
Jelescu, I.O., Budde, M.D., 2017. Design and validation of diffusion MRI models of white matter. Front. Phys. https://doi.org/10.3389/fphy.2017.00061.
Jelescu, I.O., de Skowronski, A., Geffroy, F., Palombo, M., Novikov, D.S., 2022. Neurite Exchange Imaging ((NEXI): a minimal model of diffusion in gray matter with inter-compartment water exchange. Neuroimage 256, 119277. https://doi.org/10.1016/j.neuroimage.2022.119277.
Jelescu, I.O., Veraart, J., Fieremans, E., Novikov, D.S., 2016. Degeneracy in model parameter estimation for multi-compartmental diffusion in neuronal tissue. NMR Biomed 29, 33–47. https://doi.org/10.1002/nbm.3450.
Jensen, J.H., Falangola, M.F., Hu, C., Tabesh, A., Rapalino, O., Lo, C., Helpern, J.A., 2011. Preliminary observations of increased diffusional kurtosis in human brain following recent cerebral infarction. NMR Biomed. 24, 452–457. https://doi.org/10.1002/nbm.1610.
Kaden, E., Kelm, N.D., Carson, R.P., Does, M.D., Alexander, D.C., 2016. Multi-compartment microscopic diffusion imaging. Neuroimage 139, 346–359. https://doi.org/10.1016/j.neuroimage.2016.06.002.
Kamagata, K., Hatano, T., Okuzumi, A., Motoi, Y., Abe, O., Shimoji, K., Kamiya, K., Suzuki, M., Hori, M., Kumamaru, K.K., Hattori, N., Aoki, S., 2016. Neurite orientation dispersion and density imaging in the substantia nigra in idiopathic Parkinson disease. Eur. Radiol. 26, 2567–2577. https://doi.org/10.1007/s00330-015-4066-8.
Kamiya, K., Hori, M., Aoki, S., 2020. NODDI in clinical research. J. Neurosci. Methods. https://doi.org/10.1016/j.jneumeth.2020.108908.
Kellner, E., Dhital, B., Kiselev, V.G., Reisert, M., 2016. Gibbs-ringing artifact removal based on local subvoxel-shifts. Magn. Reson. Med. 76, 1574–1581. https://doi.org/10.1002/mrm.26054.
Kellner, E., Reisert, M., Rau, A., Hosp, J., Demerath, T., Weiller, C., Urbach, H., 2022. Clinical feasibility of diffusion microstructure imaging (DMI) in acute ischemic stroke. NeuroImage Clin. 36, 103189. https://doi.org/10.1016/j.nicl.2022.103189.
Knight, M.J., Mcgarry, B.L., Rogers, H.J., Jokivarsi, K.T., Gröhn, O.H.J., Kauppinen, R.A., 2016. A spatiotemporal theory for MRI T2 relaxation time and apparent diffusion coefficient in the brain during acute ischaemia: application and validation in a rat acute stroke model. J. Cereb. Blood Flow Metab. 36, 1232–1243. https://doi.org/10.1177/0271678X15608394.
Knight, R.A., Ordidge, R.J., Helpern, J.A., Chopp, M., Rodolosi, L.C., Peck, D., 1991. Temporal evolution of ischemic damage in rat brain measured by proton nuclear magnetic resonance imaging. Stroke 22, 802–808. https://doi.org/10.1161/01.STR.22.6.802.
Kroon, D.-J., 2011. 2D line curvature and normals [WWW Document]. URL. https://www.mathworks.com/matlabcentral/fileexchange/32696-2d-line-curvature-and-normals. accessed 12 June 2024.
Kunz, N., da Silva, A.R., Jelescu, I.O., 2018. Intra- and extra-axonal axial diffusivities in the white matter: which one is faster? Neuroimage 181, 314–322. https://doi.org/10.1016/j.neuroimage.2018.07.020.
Lampinen, B., Lätt, J., Wasselius, J., van Westen, D., Nilsson, M., 2021. Time dependence in diffusion MRI predicts tissue outcome in ischemic stroke patients. Magn. Reson. Med. 86, 754–764. https://doi.org/10.1002/mrm.28743.
Lampinen, B., Szczepankiewicz, F., Lätt, J., Knutsson, L., Mårtensson, J., Björkman-Burtscher, I.M., van Westen, D., Sundgren, P.C., Ståhlberg, F., Nilsson, M., 2023. Probing brain tissue microstructure with MRI: principles, challenges, and the role of multidimensional diffusion-relaxation encoding. Neuroimage. https://doi.org/10.1016/j.neuroimage.2023.120338.
Lampinen, B., Szczepankiewicz, F., Novén, M., van Westen, D., Hansson, O., Englund, E., Mårtensson, J., Westin, C.F., Nilsson, M., 2019. Searching for the neurite density with diffusion MRI: challenges for biophysical modeling. Hum. Brain Mapp. 40, 2529–2545. https://doi.org/10.1002/hbm.24542.
Landman, B.A., Bogovic, J.A., Wan, H., ElShahaby, F.E.Z., Bazin, P.L., Prince, J.L., 2012. Resolution of crossing fibers with constrained compressed sensing using diffusion tensor MRI. Neuroimage 59, 2175–2186. https://doi.org/10.1016/j.neuroimage.2011.10.011.
Lätt, J., Nilsson, M., van Western, D., Wirestam, R., Ståhlberg, F., Brockstedt, S., 2009. Diffusion-weighted MRI measurements on stroke patients reveal water-exchange mechanisms in sub-acute ischaemic lesions. NMR Biomed. 22, 619–628. https://doi.org/10.1002/nbm.1376.
Lee, Hyunna, Lee, E.J., Ham, S., Lee, Han Bin, Lee, J.S., Kwon, S.U., Kim, J.S., Kim, N., Kang, D.W., 2020. Machine learning approach to identify stroke within 4.5 hours. Stroke 51, 860–866. https://doi.org/10.1161/STROKEAHA.119.027611.
Lin, M., He, H., Tong, Q., Ding, Q., Yan, X., Feiweier, T., Zhong, J., 2018. Effect of myelin water exchange on DTI-derived parameters in diffusion MRI: elucidation of TE dependence. Magn. Reson. Med. 79, 1650–1660. https://doi.org/10.1002/mrm.26812.
Lin, S.P., Schmidt, R.E., McKinstry, R.C., Ackerman, J.J., Neil, J.J., 2002. Investigation of mechanisms underlying transient T2 normalization in longitudinal studies of ischemic stroke. J. Magn. Reson. Imaging 15, 130–136. https://doi.org/10.1002/jmri.10052.
Lin, T.N., Sun, S.W., Cheung, W.M., Li, F., Chang, C., 2002. Dynamic changes in cerebral blood flow and angiogenesis after transient focal cerebral ischemia in rats: evaluation with serial magnetic resonance imaging. Stroke 33, 2985–2991. https://doi.org/10.1161/01.STR.0000037675.97888.9D.
Liu, H.S., Shen, H., Harvey, B.K., Castillo, P., Lu, H., Yang, Y., Wang, Y., 2011. Post-treatment with amphetamine enhances reinnervation of the ipsilateral side cortex in stroke rats. Neuroimage 56, 280–289. https://doi.org/10.1016/j.neuroimage.2011.02.049.
Mastropietro, A., Rizzo, G., Fontana, L., Figini, M., Bernardini, B., Straffi, L., Marcheselli, S., Ghirmai, S., Nuzzi, N.P., Malosio, M.L., Grimaldi, M., 2019. Microstructural characterization of corticospinal tract in subacute and chronic stroke patients with distal lesions by means of advanced diffusion MRI. Neuroradiology 61, 1033–1045. https://doi.org/10.1007/s00234-019-02249-2.
Matsumoto, K., Lo, E.H., Pierce, A.R., Wei, H., Garrido, L., Kowall, N.W., 1995. Role of vasogenic edema and tissue cavitation in ischemic evolution on diffusion-weighted imaging: comparison with multiparameter MR and immunohistochemistry. Am. J. Neuroradiol. 16, 1107–1115.
McKinnon, E.T., Jensen, J.H., 2019. Measuring intra-axonal T2 in white matter with direction-averaged diffusion MRI. Magn. Reson. Med. 81, 2985–2994. https://doi.org/10.1002/mrm.27617.
Moseley, M.E., Cohen, Y., Mintorovitch, J., Chileuitt, L., Shimizu, H., Kucharczyk, J., Wendland, M.F., Weinstein, P.R., 1990. Early detection of regional cerebral ischemia in cats: comparison of diffusion- and T2-weighted MRI and spectroscopy. Magn. Reson. Med. 14, 330–346. https://doi.org/10.1002/mrm.1910140218.
Nägele, F.L., Petersen, M., Mayer, C., Bönstrup, M., Schulz, R., Gerloff, C., Thomalla, G., Cheng, B., 2024. Longitudinal microstructural alterations surrounding subcortical ischemic stroke lesions detected by free-water imaging. Hum. Brain Mapp. 45, e26722. https://doi.org/10.1002/hbm.26722.
Nilsson, M., Alerstam, E., Wirestam, R., Ståhlberg, F., Brockstedt, S., Lätt, J., 2010. Evaluating the accuracy and precision of a two-compartment Kärger model using Monte Carlo simulations. J. Magn. Reson. 206, 59–67. https://doi.org/10.1016/j.jmr.2010.06.002.
Novikov, D.S., Fieremans, E., 2012. Relating extracellular diffusivity to cell size distribution and packing density as applied to white matter. In: Proceedings of the International Society for Magnetic Resonance in Medicine, p. 1829.
Novikov, D.S., Fieremans, E., Jespersen, S.N., Kiselev, V.G., 2019. Quantifying brain microstructure with diffusion MRI: theory and parameter estimation. NMR Biomed. https://doi.org/10.1002/nbm.3998.
Ordidge, R.J., Helpern, J.A., Knight, R.A., Qing, Z., Welch, K.M.A., 1991. Investigation of cerebral ischemia using magnetization transfer contrast (MTC) MR imaging. Magn. Reson. Imaging 9, 895–902. https://doi.org/10.1016/0730-725X(91)90533-R.
Palombo, M., Ianus, A., Guerreri, M., Nunes, D., Alexander, D.C., Shemesh, N., Zhang, H., 2020. SANDI: a compartment-based model for non-invasive apparent soma and neurite imaging by diffusion MRI. Neuroimage 215, 116835. https://doi.org/10.1016/j.neuroimage.2020.116835.
Pasternak, O., Sochen, N., Gur, Y., Intrator, N., Assaf, Y., 2009. Free water elimination and mapping from diffusion MRI. Magn. Reson. Med. 62, 717–730. https://doi.org/10.1002/mrm.22055.
Paxinos, G., Watson, C., 2004. The rat brain in stereotaxic coordinates, 5th edition, 5th ed J. Chem. Inf. Model.. https://doi.org/10.1017/CBO9781107415324.004.
Peled, S., Cory, D.G., Raymond, S.A., Kirschner, D.A., Jolesz, F.A., 1999. Water diffusion, T2, and compartmentation in frog sciatic nerve. Magn. Reson. Med. 42, 911–918. https://doi.org/10.1002/(SICI)1522-2594(199911)42:5<911::AID-MRM11>3.0.CO;2-J.
Pierpaoli, C., Righini, A., Linfante, I., Tao-Cheng, J.H., Alger, J.R., Di Chiro, G., 1993. Histopathologic correlates of abnormal water diffusion in cerebral ischemia: diffusion-weighted MR imaging and light and electron microscopic study. Radiology 189, 439–448. https://doi.org/10.1148/radiology.189.2.8210373.
Poot, D.H.J., den Dekker, A.J., Achten, E., Verhoye, M., Sijbers, J., 2010. Optimal experimental design for diffusion kurtosis. Imaging. Med. Imaging, IEEE Trans. https://doi.org/10.1109/TMI.2009.2037915.
Reisert, M., Kellner, E., Dhital, B., Hennig, J., Kiselev, V.G., 2017. Disentangling micro from mesostructure by diffusion MRI: a Bayesian approach. Neuroimage 147, 964–975. https://doi.org/10.1016/j.neuroimage.2016.09.058.
Schilling, K.G., Janve, V., Gao, Y., Stepniewska, I., Landman, B.A., Anderson, A.W., 2018. Histological validation of diffusion MRI fiber orientation distributions and dispersion. Neuroimage 165, 200–221. https://doi.org/10.1016/j.neuroimage.2017.10.046.
Sijbers, J., den Dekker, A.J., 2004. Maximum likelihood estimation of signal amplitude and noise variance from MR data. Magn. Reson. Med. 51, 586–594. https://doi.org/10.1002/mrm.10728.
Smith, S.M., Jenkinson, M., Woolrich, M.W., Beckmann, C.F., Behrens, T.E.J., Johansen-Berg, H., Bannister, P.R., De Luca, M., Drobnjak, I., Flitney, D.E., Niazy, R.K., Saunders, J., Vickers, J., Zhang, Y., De Stefano, N., Brady, J.M., Matthews, P.M., 2004. Advances in functional and structural MR image analysis and implementation as FSL. Neuroimage 23, S208–S219. https://doi.org/10.1016/j.neuroimage.2004.07.051. Supple.
Sotak, C.H., 2002. The role of diffusion tensor imaging in the evaluation of ischemic brain injury - a review. NMR Biomed. 15, 561–569. https://doi.org/10.1002/nbm.786.

Szafer, A., Zhong, J., Gore, J.C., 1995. Theoretical model for water diffusion in tissues. Magn. Reson. Med. 33, 697–712. https://doi.org/10.1002/mrm.1910330516.
Szczepankiewicz, F., Lasič, S., van Westen, D., Sundgren, P.C., Englund, E., Westin, C.F., Ståhlberg, F., Lätt, J., Topgaard, D., Nilsson, M., 2015. Quantification of microscopic diffusion anisotropy disentangles effects of orientation dispersion from microstructure: applications in healthy volunteers and in brain tumors. Neuroimage 104, 241–252. https://doi.org/10.1016/j.neuroimage.2014.09.057.
Tournier, J.D., Smith, R., Raffelt, D., Tabbara, R., Dhollander, T., Pietsch, M., Christiaens, D., Jeurissen, B., Yeh, C.H., Connelly, A., 2019. MRtrix3: a fast, flexible and open software framework for medical image processing and visualisation. Neuroimage. https://doi.org/10.1016/j.neuroimage.2019.116137.
Veraart, J., Novikov, D.S., Christiaens, D., Ades-aron, B., Sijbers, J., Fieremans, E., 2016. Denoising of diffusion MRI using random matrix theory. Neuroimage 142, 394–406. https://doi.org/10.1016/j.neuroimage.2016.08.016.
Veraart, J., Novikov, D.S., Fieremans, E., 2017. TE dependent Diffusion Imaging (TEdDI) distinguishes between compartmental T2 relaxation times. Neuroimage. https://doi.org/10.1016/j.neuroimage.2017.09.030.
Veraart, J., Nunes, D., Rudrapatna, U., Fieremans, E., Jones, D.K., Novikov, D.S., Shemesh, N., 2020. Noninvasive quantification of axon radii using diffusion MRI. Elife 9, e49855. https://doi.org/10.7554/eLife.49855.
Wagner, D.C., Deten, A., Härtig, W., Boltze, J., Kranz, A., 2012. Changes in T2 relaxation time after stroke reflect clearing processes. Neuroimage 61, 780–785. https://doi.org/10.1016/j.neuroimage.2012.04.023.
Wang, N., Zhang, J., Cofer, G., Qi, Y., Anderson, R.J., White, L.E., Allan Johnson, G., 2019. Neurite orientation dispersion and density imaging of mouse brain microstructure. Brain Struct. Funct. 224, 1797–1813. https://doi.org/10.1007/s00429-019-01877-x.
Wang, Z.Xiong, Zhu, W.Zhen, Zhang, S., Shaghaghi, M., Cai, K.Jia, 2021. Neurite orientation dispersion and density imaging of rat brain microstructural changes due to middle cerebral artery occlusion at a 3T MRI. Curr. Med. Sci. 41, 167–172. https://doi.org/10.1007/s11596-021-2332-3.
Wang, Z., Zhang, S., Liu, C., Yao, Y., Shi, J., Zhang, J., Qin, Y., Zhu, W., 2019. A study of neurite orientation dispersion and density imaging in ischemic stroke. Magn. Reson. Imaging 57. https://doi.org/10.1016/j.mri.2018.10.018.
Whittall, K.P., MacKay, A.L., Graeb, D.A., Nugent, R.A., Li, D.K.B., Paty, D.W., 1997. In vivo measurement of T2 distributions and water contents in normal human brain. Magn. Reson. Med. 37, 34–43. https://doi.org/10.1002/mrm.1910370107.
Yu, S.J., Wu, K.J., Bae, E., Wang, Y.–Syuan, Chiang, C.W., Kuo, L.W., Harvey, B.K., Greig, N.H., Wang, Y., 2020. Post-treatment with Posiphen reduces endoplasmic reticulum stress and neurodegeneration in stroke brain. iScience 23, 100866. https://doi.org/10.1016/j.isci.2020.100866.
Zhang, H., Schneider, T., Wheeler-Kingshott, C.A., Alexander, D.C., 2012. NODDI: practical in vivo neurite orientation dispersion and density imaging of the human brain. Neuroimage 61, 1000–1016. https://doi.org/10.1016/j.neuroimage.2012.03.072.
Zhang, J., Lemberskiy, G., Moy, L., Fieremans, E., Novikov, D.S., Kim, S.G., 2021. Measurement of cellular-interstitial water exchange time in tumors based on diffusion-time-dependent diffusional kurtosis imaging. NMR Biomed. 34, e4496. https://doi.org/10.1002/nbm.4496.